

Article

Quantifying the Biophysical Impact of Budding Cell Division on the Spatial Organization of Growing Yeast Colonies

Mikahl Banwarth-Kuhn , Jordan Collignon and Suzanne Sindi *

Department of Applied Mathematics, School of Natural Sciences, University of California, Merced, CA 95343, USA; mbanwarth-kuhn@ucmerced.edu (M.B.-K.); jcollignon@ucmerced.edu (J.C.)

* Correspondence: ssindi@ucmerced.edu

Received: 17 July 2020; Accepted: 13 August 2020; Published: 20 August 2020



Abstract: Spatial patterns in microbial colonies are the consequence of cell-division dynamics coupled with cell-cell interactions on a physical media. Agent-based models (ABMs) are a powerful tool for understanding the emergence of large scale structure from these individual cell processes. However, most ABMs have focused on fission, a process by which cells split symmetrically into two daughters. The yeast, *Saccharomyces cerevisiae*, is a model eukaryote which commonly undergoes an asymmetric division process called budding. The resulting mother and daughter cells have unequal sizes and the daughter cell does not inherit the replicative age of the mother. In this work, we develop and analyze an ABM to study the impact of budding cell division and nutrient limitation on yeast colony structure. We find that while budding division does not impact large-scale properties of the colony (such as shape and size), local spatial organization of cells with respect to spatial layout of mother-daughter cell pairs and connectivity of subcolonies is greatly impacted. In addition, we find that nutrient limitation further promotes local spatial organization of cells and changes global colony organization by driving variation in subcolony sizes. Moreover, resulting differences in spatial organization, coupled with differential growth rates from nutrient limitation, create distinct sectoring patterns within growing yeast colonies. Our findings offer novel insights into mechanisms driving experimentally observed sectored yeast colony phenotypes. Furthermore, our work illustrates the need to include relevant biophysical mechanisms when using ABMs to compare to experimental studies.

Keywords: budding; yeast; agent-based model; microbial colonies; spatial organization; Hertz potential

1. Introduction

The morphological characteristics exhibited by growing microbial communities arise from complex interactions between genetic, epigenetic, environmental and cellular determinants [1–14] (Figure 1). For example, the emergence of large regions of a single genotype in bacterial colonies is most often associated with the chance loss of certain genes as individuals die or do not reproduce due to nutrient limitation [8,9,11]. In this scenario, the survival or extinction of an individual depends on relative fitness or physical interactions with neighboring cells [5]. In yeast colonies, sectoring patterns appear when cells transition between different phenotypic states [2,3,15–21]. One example in *Saccharomyces cerevisiae* is the appearance of sectoring in yeast prion phenotypes. In the non-prion state ($[psi^-]$), cells establish red colonies; however, when prion aggregates are present ($[PSI^+]$), *S. cerevisiae* colonies exhibit different colors ranging from white (strong) to shades of pink (weak). Under certain experimental conditions, changes in protein aggregation dynamics between neighboring cells result in sectors corresponding to loss of the prion phenotype (Figure 1D).

Other examples of sectoring in yeast colonies include spontaneous mitotic crossover [18,19] and the white-opaque switch in *Candida albicans* [2,16,17,20,21]. In each case, the complex phenotypic organization that arises from an initially small group of cells, provides a rich data set that can be used to uncover relationships between molecular processes, individual cell behaviors and phenotypic transitions at the colony level (Figure 1). At this point, most biological studies do not provide rigorous quantification of shape, size and structure between different sectoring phenotypes. As such, characterizing the role of individual cell behaviors in directing spatial organization of cells, as well as quantifying their impact on overall heterogeneity and disease progression within microbial communities is an underexplored opportunity for discovery. In this study, we propose a novel mathematical and computational framework that depicts realistic biophysical division processes and the effect of nutrient limitation, and use our model to study how these processes impact colony organization.

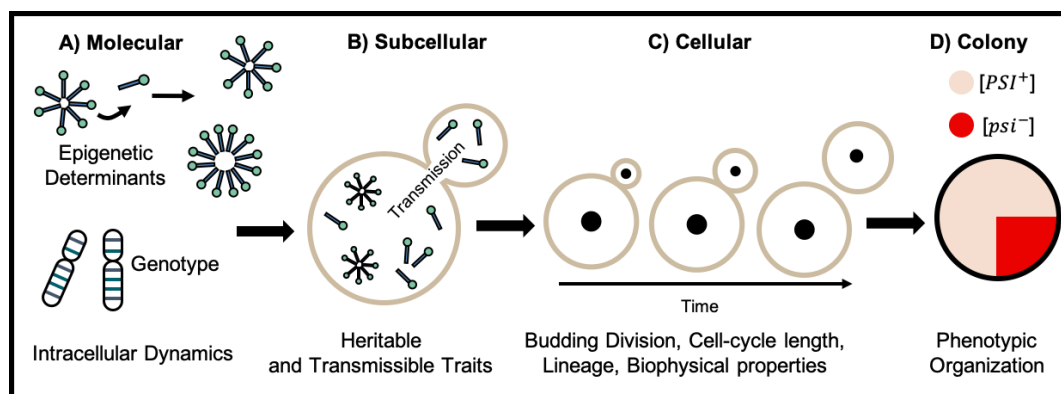


Figure 1. Spatial Phenotypes are the Consequence of Processes at Different Scales. (A) Cells transition between different phenotypic states due to genetic mutations or epigenetic determinants. For example, alternative conformations of the prion protein in *S. cerevisiae* can function as epigenetic determinants of transmissible phenotypes. (B) Daughter cells inherit their phenotype from their mother. In some cases, inefficient transmission of different intracellular constituents (i.e., prion aggregates) can lead to loss of phenotype. (C) Individual cell behaviors impact the propagation, loss and spatial arrangement of phenotypes within the colony. In this paper we investigate the impact of budding division in *S. cerevisiae* on overall shape, size and spatial organization of cells. During budding division, the new daughter cell forms as a bud on the mother cell and remains attached until it reaches a mature size and they physically separate. (D) The outcome of processes at the molecular, subcellular and cellular scales lead to different morphological traits such as sector-like regions in *S. cerevisiae* colonies where all cells have lost the prion phenotype.

In yeast, and other microbial colonies, cells grow closely together, and the cumulative effect of mechanical interactions at the microscopic scale impacts the overall shape and organization of growing colonies [5,22]. For example, patterns of polarized growth and division have been shown to impact cellular organization, and cell-cell adhesion forces have been shown to impact how the population expands outward and how cells divide [23]. An interesting feature of *S. cerevisiae* is that cells undergo an asymmetric division process called budding (Figures 1 and 14) [24–28]. During budding division, new daughter cells form as protrusions on the surface of the mother cell and stay attached until they reach a mature size and physically separate. After separation the resulting mother and daughter cells are unequal in size and the daughter cell does not inherit the replicative age of the mother. The creation of a large mother-daughter cell pair during budding division results in distinct biophysical properties from fission (i.e., non-budding division), a process by which cells split symmetrically into two daughters. Moreover, this difference leads to small perturbations in the physical interaction between neighboring cells and could act as a mechanism driving emergent patterns of organization. Thus, in the case of *S. cerevisiae*, understanding the impact of budding division and other individual

cell behaviors on spatial relationships between cells may be paramount to understanding the evolution of phenotypic organization such as prion sectors.

In addition to biophysical properties of cells, an environmental factor that impacts cell behaviors is nutrient limitation [8,11,29–32]. Namely, the availability of required nutrients limits cell growth progression consequently slowing or stopping reproduction [11]. Regulatory pathways governing growth and quiescence in yeast cells are well-studied [33,34]. Combined experimental and computational studies suggest that nutrient limitation is a key mechanism driving the emergence of organizational structures in growing microbial communities [8,29]. In addition, Nadell et al. [29] used an agent-based model (ABM) to investigate the impact of physical and biological parameters, including nutrient availability, on the spatial distribution of genetic lineages within microbial colonies. Recent studies provide further evidence that biophysical properties of cells can influence cell-cell interactions and change organizational dynamics within the colony [5,35–37]. For example, Giometto et al. [5] showed that physical interactions of cells prolong the survival of less-fit strains at the growing frontier of *S. cerevisiae* colonies. While these studies provide compelling evidence that mechanical properties of cells and nutrient limitation serve as a combined mechanism driving spatial organization in microbial colonies, quantifying their individual impact in experiments is very difficult.

Mathematical and computational models have served as successful tools for investigating the role of individual cell behaviors and mechanical properties of cells on emergent patterns in multicellular tissues and growing microbial colonies. For example, cell-based models have been successfully used to capture passive biomechanical properties of cells during tissue development (for reviews see References [38,39]) as well as microbial biofilm formation [40]. However, computational models that focus on the impact of individual cell behaviors in directing spatial organization of yeast colonies is somewhat limited. Jönsson et al. [41] proposed an ABM to study the effect of cell division patterns and growth inhibition by neighboring cells on variations in the size and shape of growing *S. cerevisiae* colonies. In addition, Wang et al. [42] developed an ABM with several important biological processes including budding division, mating, mating type switch, consumption of nutrients, and cell death. They used their model to study the impact of different budding patterns and nutrient limitation on mating probabilities, colony development and colony expansion. In each of these previous studies, results focused on the colony as a whole—size, shape and expansion—and not how the colony itself was organized. An additional set of studies used ABMs to investigate the impact of individual cell growth and reproduction times on colony expanse as well as study the relationship between cell generation and birth location in the colony [43–47]. However, likely for computational simplicity, these prior studies focused primarily on populations of a few hundred or few thousand cells. To our knowledge, this represents the first biophysical model designed to study budding colonies that considers populations of more than 10,000 cells and emphasizes the impact of biophysical properties of cells on colony organization.

In this paper, we study the impact of budding cell division on overall shape, size and spatial organization of growing yeast colonies. To do this, we develop a 2D ABM that explicitly includes the mechanical interactions that arise when the daughter cell is growing and physically connected to its mother. Spatial rearrangement of cells in our synthetic colonies depends on cell-cell interaction and our model incorporates several other important biological processes including, asymmetric cell cycle lengths between the mother and daughter cell and the impact of nutrient limitation. In addition, we develop specific metrics to quantify the spatial organization of cells that emerges due to different biophysical properties in budding and non-budding colonies. We then adapt our model to simulate colony growth in a nutrient-rich and nutrient-limited environment and discuss how nutrient limitation impacts global colony organization as it relates to sector-like regions formed by individual subcolonies. In Section 2.1 we analyze the impact of budding alone by considering colonies grown in an environment with an inexhaustible supply of nutrients. In Section 2.2 we study how a more realistic nutrient-limited environment acts in concert with biophysical forces created by budding division to further impact colony organization. In Section 3 we discuss the implications of

our work in understanding the appearance of sectoring patterns in growing yeast colonies and more broadly outline extensions of our model to further study prion sectors in *S. cerevisiae*. In Section 4, a detailed description of our model and the metrics we developed to quantify spatial organization of cells are given. Finally, Section 5 offers our concluding remarks.

2. Results

To study the impact of budding division on the spatial organization of *S. cerevisiae* colonies, we developed a 2D computational model to compare morphological characteristics and spatial arrangement of cells between budding and non-budding colonies in both nutrient-rich and nutrient-limited conditions (see Section 4 for a detailed discussion of our computational model and the metrics we use to evaluate our colonies). Note, by non-budding colonies we mean colonies where mother-bud pairs are not physically attached while the new daughter grows to a mature size. In the model, we represent each cell by an elastic sphere that moves, grows, buds and divides according to biophysical and cell-kinetic model parameters chosen to match experimentally derived values (Section 4.1, Table 1, Figures 12–14). Each simulation begins with a single newly born founder cell. We allow the colony to grow for ≈ 24 h until there are $\approx 15,000$ cells. We compared our synthetic yeast colonies grown under different conditions (budding/non-budding, nutrient-rich/nutrient-limited) with metrics designed to capture the overall colony growth, shape, and spatial organization of cells (see Section 4.2). Results below are based on 50 simulations for each of these four conditions. Typical output from budding and non-budding colonies in nutrient-rich conditions is shown in Figure 2 (middle and bottom rows) and typical output from budding and non-budding colonies in nutrient-limited conditions is shown in Figure 11A–D.

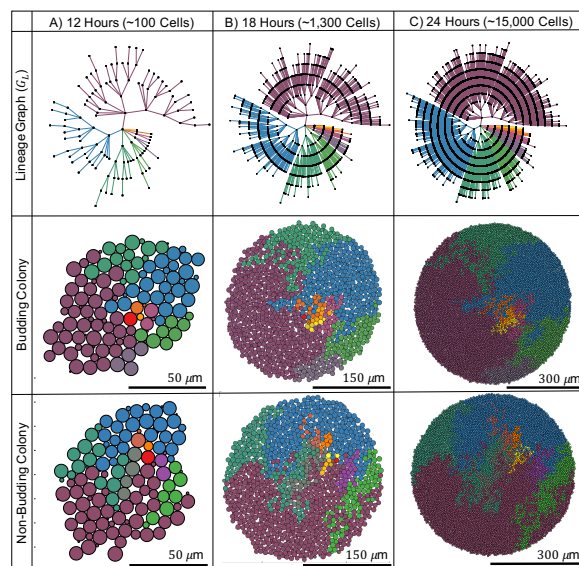


Figure 2. Simulated Yeast Colonies in Nutrient-Rich Conditions and Corresponding Lineage Relationships. We compared overall growth, shape and spatial organization between budding (Middle) and non-budding (Bottom) colonies. Colonies are depicted at three time points (A) 12 h (~ 100 cells); (B) 18 h (~ 1300 cells) and (C) 24 h ($\sim 15,000$ cells). In addition to the physical layout of cells, we analyzed two different networks associated with our colonies, the lineage graph (G_L , Top) and the spatial graph (G_S , see Section 4.2.2). (Top row) The lineage graph (G_L) represents mother-daughter relationships and does not consider cell position in space. As such, the lineage graph is the same for the two different colonies depicted below (budding and non-budding). Cells in colonies and edges in the lineage graph are colored according to the unique subcolony each cell belongs to, where a **subcolony** is the subset of all cells whose common ancestor is the same immediate daughter of the founder cell: Founder (red), Subcolony 1 (maroon), Subcolony 2 (blue), Subcolony 3 (dark green), Subcolony 4 (light green), Subcolony 5 (lavender), Subcolony 6 (purple), Subcolony 7 (dark orange), Subcolony 8 (gold), Subcolony 9 (yellow), Subcolony 10 (rust), Subcolony 11 (magenta), Subcolony 12 (light pink) and Subcolony 13 (grey). Lineage graphs display the first five subcolonies only. (See Section 4.2.2 for details.)

As we next discuss in greater detail, we find that metrics corresponding to the overall growth and shape of colonies are not impacted by budding division. However, we observe significant differences in metrics characterizing the local spatial organization and connectivity of budding versus non-budding colonies. Finally, we find that in addition to further impacting local spatial organization and colony connectivity, nutrient limitation changes the global organization of growing yeast colonies.

2.1. Nutrient-Rich Growth: Budding Division Impacts Local Colony Organization in Simulated Yeast Colonies

First, we consider colonies growing in “nutrient-rich” conditions. As described in Section 4.1.1, for budding colonies, we explicitly model the mechanical interactions that arise due to the formation of a new daughter cell from budding (Figure 12A). When simulating non-budding colonies, we treat mechanical interactions of mother-bud pairs and all other cell-cell pairs identically (Section 4.1.1 and Figure 12B).

2.1.1. Budding Does Not Impact Large-Scale Colony Growth or Structure (Expanse or Sparsity)

In the absence of nutrient limitation, colony growth is exponential with a doubling time of ~ 105 min. More specifically, mother cells have a doubling time of ~ 90 min and new daughter cells have a doubling time of ~ 120 min. Figure 3A and Figure 14). We assume no difference in growth rate or cell cycle length between budding and non-budding colonies. Thus, as expected, we see no difference in total population between budding and non-budding colonies (Figure 3A).

Next, we compared the size and shape of budding and non-budding colonies under nutrient-rich conditions by calculating the expanse and sparsity of each colony (Figure 3B,C). The expanse quantifies how large the colony is with respect to the average distance of each cell to the colony center of mass, while colony sparsity is a measure that quantifies the roundness of each colony (Section 4.2.1). As the colony grows, the colony expanse increases and the colony sparsity decreases towards 1, implying that the colony is becoming more circular as the number of cells in the colony increases. We observe no difference between colony expanse or colony sparsity between budding and non-budding colonies (Figure 3B,C). Thus, budding does not impact the appearance of the colony when viewed as a whole.

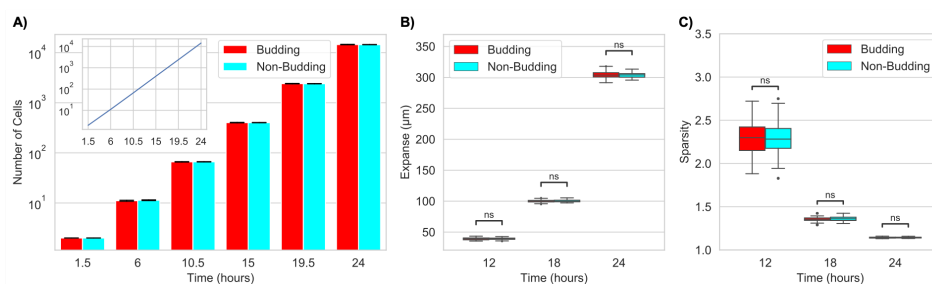


Figure 3. Population Growth, Expanse and Sparsity of Simulated Yeast Colonies in Nutrient-Rich Conditions. (A) Colony growth is exponential with doubling time ~ 105 min (inset). Bar plots represent average number of cells in each colony across all 50 simulations for both budding and non-budding colonies under nutrient-rich conditions calculated at 4.5 h intervals; (B) Colony expanse increases over time for both budding and non-budding colonies; (C) Colony sparsity decreases to 1 (implying that the colony is becoming more circular) as the size of the colony increases over time for both budding and non-budding colonies. (See Section 2.1.1 for details.)

2.1.2. Budding Does Not Change Global Age and Spatial Structure but Impacts Local Connectivity

Next we analyzed the relationship between cell age and spatial location within the colony after 24 h of growth. First we computed the empirical probability density function for the ages of cells in the colony (Figure 4A). We find that over 93% of cells are less than 8 h old, and thus we focus on this subpopulation. (Note, because cell cycle timing is unchanged between budding and non-budding colonies, as expected we find no difference in the distribution of cell ages between these two conditions).

Next, we quantified the birth location of cells within the colony (Figure 4B). To do this, we analyzed the empirical probability density function for the normalized distance from the colony center of mass to the birth location of cells born in the last hour of colony growth. We observe that in both conditions, cells are more likely to be born closer to the perimeter of the colony. We note that this empirical distribution has a nearly linear increase, consistent with a uniform probability per area of the colony, with the exception of the decreased probability at the moving front of the colony. Similarly, we find no difference in birth location of cells between budding and non-budding colonies demonstrating that the budding mechanism has no impact on birth locations within the colony. Finally, to ensure that this distribution itself is not age structured, we examined the distance from the colony center of mass (Figure 4C) and note that both budding and non-budding cells display uniform probabilities with respect to distance from the colony center of mass for all ages.

While there are no differences in the large-scale age structure between budding and non-budding colonies, we note that there are significant differences within the local neighborhood of a cell. More specifically, we observed a small, but statistically significant (non-overlapping 95% confidence intervals) difference in the distance a cell less than 8 h old was from its mother (Figure 4D). Although this difference is quite small (less than the average radius of a cell), because most cells in the colony fall into this age group, this suggests significant differences in the local spatial arrangement and organization of budding versus non-budding colonies. Note, for both average distance from the colony center of mass (Figure 4C) and average distance from cells to their mother (Figure 4D), average values were determined for different age groups using a sliding window with a fixed window size of 20 min. In addition, 95% confidence intervals are shown for each window.

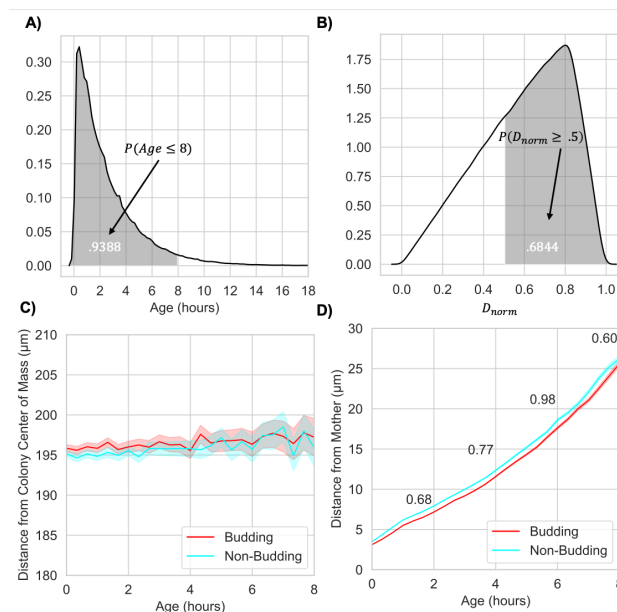


Figure 4. Age and Spatial Organization of Cells in Nutrient-Rich Colonies. (A) Empirical probability density function for cell ages in synthetic colonies after 24 h of colony growth. We observe that the probability that a given cell is ≤ 8 h old is 0.9388; (B) Empirical probability density function for the normalized distance from the colony center of mass to the birth location of cells born in the last hour of colony growth (D_{norm}). We observe that the probability that D_{norm} is ≥ 0.5 is 0.6844; (C) Cell age (h) versus cell distance from the colony center of mass for budding (red) and non-budding (blue) colonies at the 24 h time point. In both (C,D), average values were determined for different age groups using a sliding window with a fixed window size of 20 min. We conclude that cell distance from the colony center of mass is not impacted by cell age or budding division since 95% confidence intervals overlap; (D) Cell age (h) versus cell distance from its mother for budding (red) and non-budding (blue) colonies. The difference between budding and non-budding colonies is given for age groups 2,4,6,8. We conclude that this difference is significant since 95% confidence intervals do not overlap. (See Section 2.1.2 for details).

2.1.3. Budding Division Maintains Closeness between Mothers and Daughters after Physical Separation

To better quantify the differences in local spatial arrangement and organization between budding and non-budding colonies, we analyzed the spatial graph (G_S) and lineage graph (G_L) for each colony. The spatial graph has an edge between cells that are adjacent according to the Delaunay triangulation of their centers. (Figure 16A). The lineage graph has an edge between mother and daughter cell pairs regardless of their spatial position (Figure 2 (top row) and Figure 16B). We construct both graphs from our simulation output following the procedures defined in Section 4.2.2. Together, these graphs provide a framework to quantify how spatial relationships between mother-daughter cell pairs dynamically evolve during colony growth.

Colony connectivity is a measure of how many mother-daughter cell pairs are adjacent in the colony. We determine this by looking at the fraction of mother-daughter edges in G_S . (See Section 4.2.2 for more details.) First, we compared colony connectivity between budding and non-budding colonies after 12, 18 and 24 h of growth (Figure 5A). While colony connectivity decreases over time for both budding and non-budding colonies, it is significantly higher in budding colonies starting after 18 h of growth. We hypothesized that since cells in budding colonies remain physically attached to their mother until separation, high connectivity of the cells still attached to their mother could explain the observed difference. To investigate this hypothesis, we compared the connectivity between mother-daughter cell pairs in two distinct phases: when they are attached during budding cell division (“budded cells”, Figure 5B) and after separation (“un-budded cells”, Figure 5C). We observe that the connectivity of budding colonies is significantly higher in each phase (Figure 5B,C). Namely, in the case of budded cells, connectivity stays close to 1 during the entire 24 h time period for budding colonies whereas it decreases between 12–18 h and then again between 18–24 h for non-budding colonies (Figure 5B). Surprisingly, in the case of un-budded cells, the difference in connectivity is significantly different between budding and non-budding colonies starting at 18 h (Figure 5C). In fact, the absolute difference in mean connectivity between budding and non-budding colonies remains unchanged from the overall colony connectivity computed for all cells.

To further address the mechanism driving our observed differences in colony connectivity between budding and non-budding colonies, we hypothesized that mother-daughter cell pairs remain physically close for a longer period of time after separation in budding colonies. To investigate this hypothesis, we generated Kaplan-Meier survival curves for the lifetime of mother-daughter edges in G_S (lifetime being the length of time after separation). We observe that the probability that a given mother-daughter edge will remain in G_S for longer than t hours after separation is higher for budding colonies (Figure 5D). In addition, the restricted mean survival time for a given mother-daughter edge in G_S is 80 min compared to 66 min for non-budding colonies. Furthermore, we observe distinctly different behavior between the two survival curves from 0–50 min after separation, whereas after 50 min, the two curves display more similar behavior. This change in behavior is marked by a “sharp” decrease in survival probability for both types of colonies. The timing of this sharp decrease is consistent with the appearance of a second bud from the mother cell and we conjecture that the new bud “pushes away” the previous daughter.

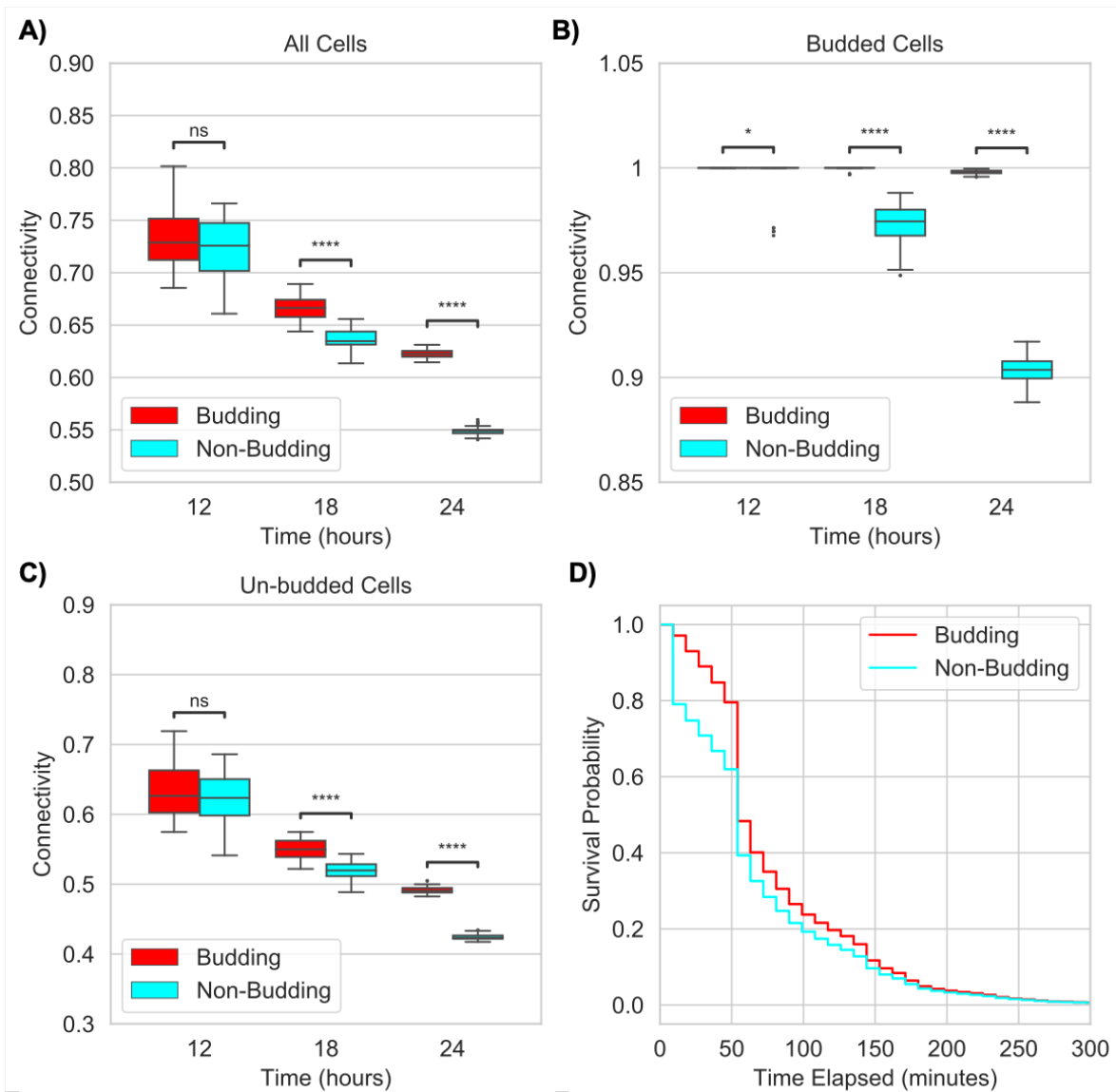


Figure 5. Colony Connectivity in Nutrient-Rich Colonies. Comparison of colony connectivity between budding (red) and non-budding (blue) colonies at 12, 18 and 24 h. We compared connectivity for all cells in (A), as well as cells in two distinct phases: during the time when cells are attached for budding colonies in (B) and after separation in (C). (See Section 4.2.2 for how we define connectivity.) (A) We observe a statistically significant difference in colony connectivity at 18 h ($p = 1.423 \times 10^{-27}$) and 24 h ($p = 2.008 \times 10^{-99}$). (B) We observe a rapid decrease in connectivity between both 12–18 and 18–24 h in non-budding colonies. This decrease leads to a statistically significant difference between budding and non-budding colonies at 12 h ($p = 3.387 \times 10^{-02}$), 18 h ($p = 6.521 \times 10^{-34}$) and 24 h ($p = 2.867 \times 10^{-103}$). (C) We observe a statistically significant difference in connectivity at 18 h ($p = 3.684 \times 10^{-19}$) and 24 h ($p = 7.615 \times 10^{-89}$). (p -values for connectivity were computed using independent t -tests. p -value annotation is as follows. *: $1.0 \times 10^{-2} \leq p \leq 5.0 \times 10^{-2}$, **: $1.0 \times 10^{-3} \leq p \leq 1.0 \times 10^{-2}$, ***: $1.0 \times 10^{-4} \leq p \leq 1.0 \times 10^{-3}$, ****: $p \leq 1.0 \times 10^{-4}$.) (D) Kaplan-Meier survival curves for the edge connecting mother-daughter cell pairs in G_S for budding (red) and non-budding (blue) colonies. The y -axis is the probability that a given mother-daughter edge will remain in G_S for longer than t hours after separation, where time is on the x -axis. We observe that the survival curves are different between the two groups ($p = 7.217 \times 10^{-25}$), indicating that the probability that a mother-daughter edge remains in G_S for longer than t hours is greater for budding colonies. (The p -value comparing survival curves was calculated using a log-rank test as described in Section 4.3.) (See Section 2.1.3 for details.)

2.1.4. Budding Division Promotes Subcolony Connectivity

Next, we considered the impact of budding division on subcolony structure and organization. We define a **subcolony** to be the subset of all cells whose common ancestor is the same immediate daughter of the founder cell (Section 4.2.2 and Figure 17). Note that a colony has as many subcolonies as immediate daughters of the founding cell. We then analyze how well each of these subcolonies is connected in terms of the spatial layout of the colony. To do this, we considered colonies at the final time point (24 h) and compared the number of connected components of the first five subcolonies between budding and non-budding division conditions. We found that the average number of connected components was significantly lower for budding colonies (Figure 6A). This demonstrates that budding division acts as a mechanism to increase spatial adjacency within subcolonies as well as impact overall subcolony connectivity.

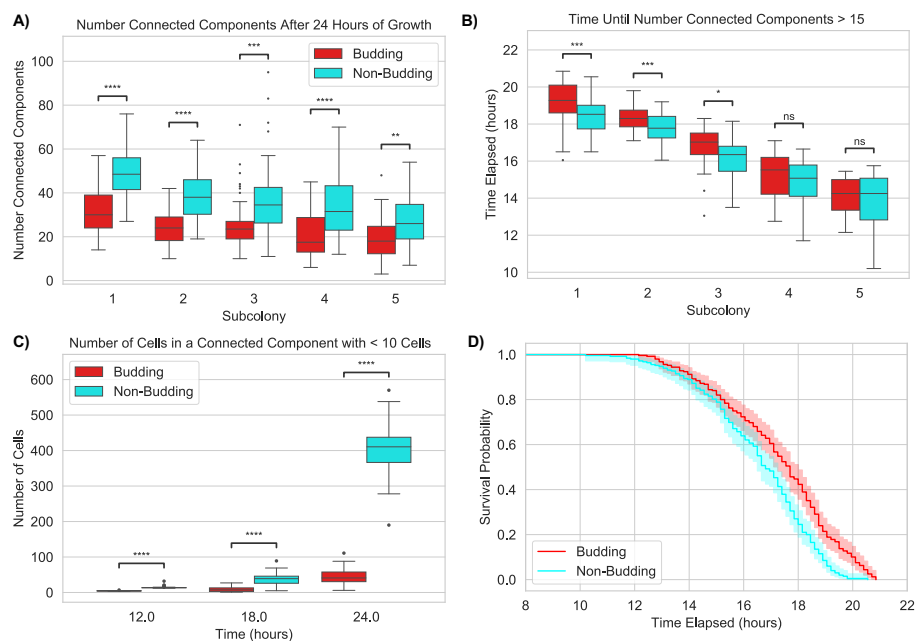


Figure 6. Subcolony Structure and Organization in Nutrient-Rich Colonies. (A) Comparison of the number of connected components for the first five subcolonies between budding (red) and non-budding (blue) colonies at the 24 h time point. We observe a statistically significant difference in the number of connected components for subcolony 1 ($p = 2.885 \times 10^{-10}$), subcolony 2 ($p = 1.139 \times 10^{-10}$), subcolony 3 ($p = 3.075 \times 10^{-04}$), subcolony 4 ($p = 1.539 \times 10^{-06}$) and subcolony 5 ($p = 1.959 \times 10^{-03}$). (B) Comparison of time from creation until each of the first five subcolonies splits into 15 connected components. We observe a statistically significant difference between budding (red) and non-budding (blue) colonies for subcolony 1 ($p = 1.140 \times 10^{-04}$), subcolony 2 ($p = 4.727 \times 10^{-04}$), and subcolony 3 ($p = 1.581 \times 10^{-02}$). (C) Comparison of the number of cells in a connected component with less than 10 cells. Note that overall very few cells are in small connected components; however, we observe a statistically significant difference between budding (red) and non-budding (blue) colonies at 12 h ($p = 7.408 \times 10^{-40}$), 18 h ($p = 7.896 \times 10^{-19}$) and 24 h ($p = 1.233 \times 10^{-59}$). (p -values in (A–C) were computed using independent t -tests. p -value annotation is as follows. *: $1.0 \times 10^{-2} \leq p \leq 5.0 \times 10^{-2}$, **: $1.0 \times 10^{-3} \leq p \leq 1.0 \times 10^{-2}$, ***: $1.0 \times 10^{-4} \leq p \leq 1.0 \times 10^{-3}$, ****: $p \leq 1.0 \times 10^{-4}$.) (D) Kaplan-Meier survival curves for the length of time a subcolony is made up of less than 15 connected components for budding (red) and non-budding (blue) colonies. The y -axis is the probability that a subcolony consists of less than 15 connected components for longer than t hours, where time is on the x -axis. We observe that the survival curves are different between the budding and non-budding colonies ($p = 1.165 \times 10^{-06}$), indicating that budding promotes subcolony connectivity. (The p -value comparing survival curves was calculated using a log-rank test as described in Section 4.3. In addition, 95% confidence intervals for the survival function are shown. See Section 2.1.4 for details.)

Because every subcolony begins with a single cell, which is necessarily a single connected component, we studied at what time a given subcolony would break apart. To do this, we computed the average time elapsed from creation of a given subcolony until it splits into more than 15 connected components. We observe that the average time was significantly lower in non-budding colonies for subcolonies 1, 2 and 3 (Figure 6B). These results suggest budding division impacts subcolony connectivity by ensuring cells in the same subcolony remain physically closer together for a longer period of time. Moreover, we hypothesized that the absence of budding division makes it easier for individual cells to become separated from the rest of their subcolony. To test this hypothesis, we computed the average number of cells in small connected components (i.e., less than 10 cells) for budding and non-budding colonies. We find that the average number of cells in a small connected component was significantly higher in non-budding colonies (Figure 6C).

In addition, we generated Kaplan-Meier survival curves for the time elapsed from creation of a subcolony to when it splits into more than 15 components. We considered this a separate event for each of the first 5 subcolonies and each of our 50 simulations. We found that the survival curves are different between the two groups (Figure 6D) indicating that the probability that a given subcolony remains connected (i.e., less than 15 connected components) for longer than t hours is greater for budding colonies.

2.2. Nutrient-Limited Growth: Differential Growth Rates Impact Global Organization of Yeast Colonies

Prior studies have shown that nutrient limitation impacts patterns of growth and spatial organization in microbial colonies [5,8,29,42]. To investigate the role of nutrient limitation and budding division together on patterns of growth and organization in our simulated yeast colonies, we revised our ABM to include nutrient-limited growth (Section 4.1.4) and used the same set of metrics as before to compare overall shape, size and spatial organization of cells. Rather than directly model the concentration of a nutrient in time as has been done previously [8,29,42,48–53], we consider regions of the growth media to have a maximal possible biomass (i.e., carrying capacity) and decrease the cell growth progression of cells in each region accordingly. In particular, we provide a simplified model of nutrient dynamics that only considers the indirect effect of nutrients on cell cycle length and does not directly model nutrient concentration or a particular type of nutrient.

2.2.1. Nutrient Limitation Slows Colony Growth but Does Not Change Large-Scale Colony Structure

As in our nutrient-rich condition, large-scale behavior (doubling time, sparsity and expanse) between budding and non-budding colonies is the same. (Figure 7A–C). However, when nutrients are limited, our synthetic yeast colonies grow slower. Since colony connectivity and structure of subcolonies significantly changes between 1000 and 10,000 cells, we computed each of our metrics for nutrient-limited colonies at an additional time point (28 h) where the number of cells in the colonies is over 10,000 and more similar to the nutrient-rich case ($\sim 12,500$ cells after 28 h of growth in nutrient-limited conditions compared to $\sim 15,000$ cells after 24 h of growth in nutrient-rich conditions). The average doubling time of a colony increases from ~ 105 min under nutrient-rich conditions to ~ 123 min in nutrient-limited conditions (Figure 7A). The colony expanse at 24 h decreases from $300 \mu\text{m}$ in nutrient-rich conditions to $150 \mu\text{m}$ in nutrient-limited conditions (Figure 7B). Similarly to nutrient-rich growth, colony sparsity decreases toward 1, indicating the colony becomes more circular as it grows (Figure 7C). Finally, as we assumed no difference in growth rate or cell cycle length between budding and non-budding division, these gross colony level metrics remain unchanged when comparing between division conditions.

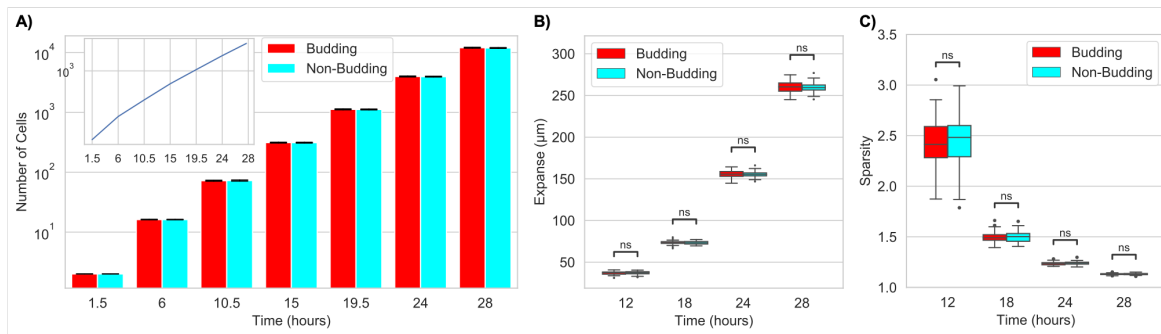


Figure 7. Population Growth, Expanse and Sparsity of Simulated Yeast Colonies in Nutrient-Limited Conditions. (A) Colony growth is exponential with doubling time ~ 123 min (inset). Bar plots represent average number of cells in each colony across all 50 simulations for both budding and non-budding colonies under nutrient-limited conditions calculated at 4.5 h intervals; (B) Colony expanse increases over time for both budding and non-budding colonies; (C) Colony sparsity decreases to 1 as the size of the colony increases over time for both budding and non-budding colonies. (See Section 2.2.1 for details.)

2.2.2. Nutrient Limitation Creates Age-Structured Colonies by Promoting Birth at the Colony Boundary

First, as in the nutrient-rich condition, the asymmetric cell cycle means that the age distributions are shifted toward younger cells in nutrient-limited colonies. Because we grow nutrient-limited colonies for a longer period (28 h vs. 24 h for nutrient-rich colonies), we consider “young cells” as those less than 12 h old (over 94% of cells in the colony). Similarly to the nutrient-rich condition, we found no difference in cell ages between budding and non-budding colonies (Figure 8A). Next, and in contrast to nutrient-rich conditions, when the cell cycle is tied to locally available nutrients the age structure of the colony changes substantially. As shown in Figure 8B, cells are far more likely to be born closer to the edge of the colony than in nutrient-rich colonies. When we observe the age structure in greater detail, we observe that the distance from the colony center of mass at 28 h is strongly correlated with age (Figure 8C). However, this relationship between age-structure and distance is unaffected by budding division. As such, we conclude that within a given growth condition, budding division does not modify the age-structure within a colony.

Similarly to nutrient-rich growth, we observe that budding division influences the local neighborhood of a cell. More specifically, we observe a small, but statistically significant (non-overlapping 95% confidence intervals) difference, in the distance a cell less than 12 h old is from its mother (Figure 8D). While this difference remains small, it is interesting that the absolute difference between budding and non-budding mother-daughter cell pairs is larger for nutrient-limited colonies and may even be increasing with the age of the daughter cell. Because colonies grown in nutrient-limited conditions are smaller than nutrient-rich colonies, this difference becomes even larger when it is considered relative to the size of the colony.

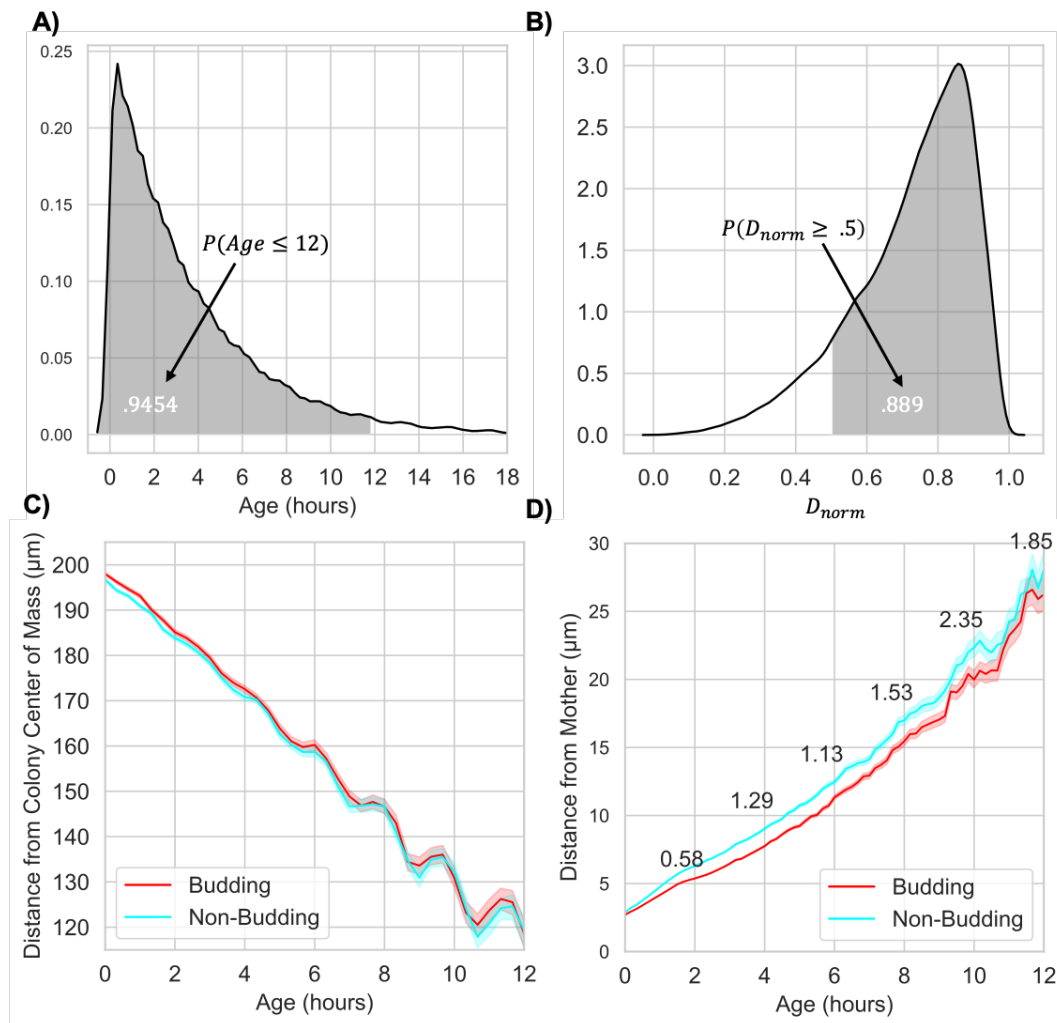


Figure 8. Age and Spatial Organization of Cells in Nutrient-Limited Colonies. (A) Empirical probability density function for cell ages in synthetic colonies after 28 h of colony growth. We observe that the probability that a given cell is ≤ 12 h old is 0.9454; (B) Empirical probability density function for the normalized distance from the colony center of mass to the birth location of cells born in the last hour of colony growth (D_{norm}). We observe that the probability that D_{norm} is ≥ 0.5 is 0.889; (C) Cell age (h) versus cell distance from the colony center of mass for budding (red) and non-budding (blue) colonies at the 28 h time point. In both (C,D) average values were determined for different age groups using a sliding window with a fixed window size of 20 min. We conclude that distance from the colony center of mass at 28 h is strongly correlated with age. However, we see that cell distance from the colony center of mass is not impacted by budding division since 95% confidence intervals overlap; (D) Cell age (h) versus cell distance from its mother for budding (red) and non-budding (blue) colonies. The difference between budding and non-budding colonies is given for ages 2, 4, 6, 8, 10 and 12. We conclude that this difference is significant since 95% confidence intervals do not overlap. Moreover, since nutrient-limited colonies are smaller than nutrient-rich colonies, this difference becomes even larger when it is considered relative to the size of the colony. (See Section 2.2.2 for details.)

2.2.3. Nutrient-Limited Growth Promotes Colony Connectivity

As for nutrient-rich growth conditions, the colony connectivity decreases in time and is significantly higher in budding colonies (compare Figure 5A with Figure 9A). However, we observe that nutrient-limited growth promotes colony connectivity as both budding and non-budding colonies have higher connectivity in this growth condition at the 24 h time point. In addition, the difference in colony connectivity is observable much earlier on in the life of the colony (12 h vs. 18 h).

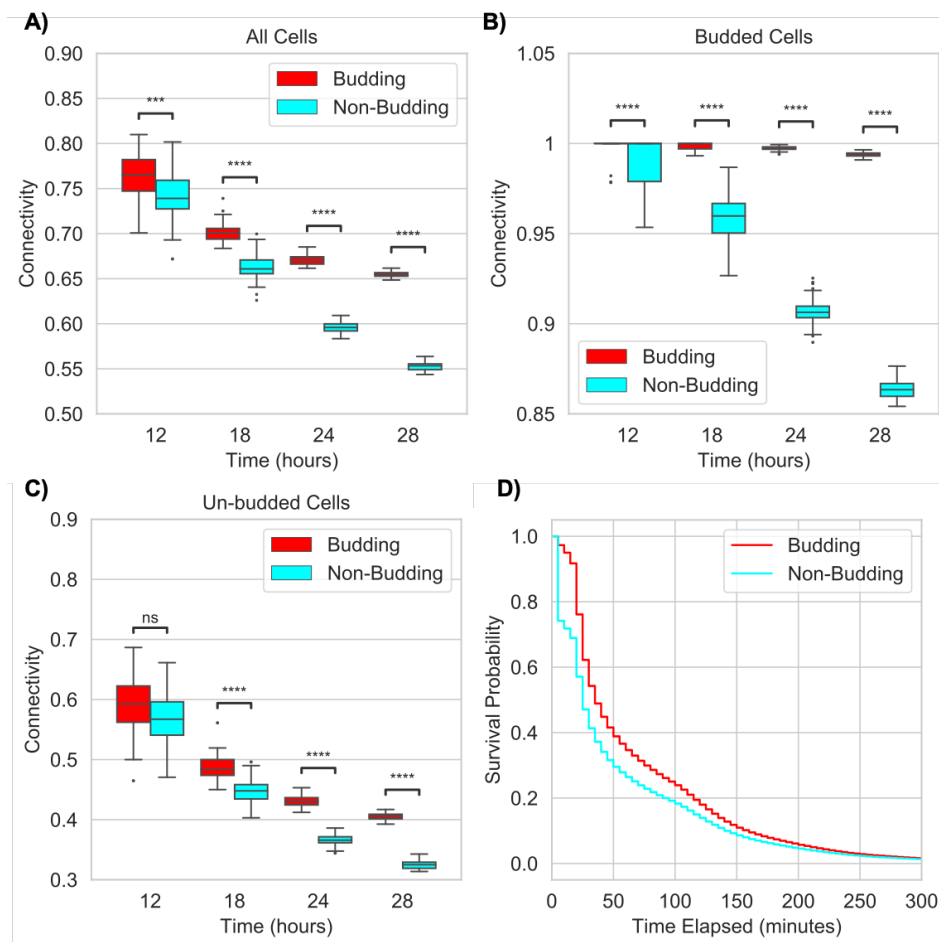


Figure 9. Colony Connectivity in Nutrient-Limited Colonies. Comparison of colony connectivity between budding and non-budding colonies in nutrient-limited conditions at 12 h, 18 h, 24 h and 28 h. We compared connectivity for all cells in (A), as well as cells in two distinct phases: during the time when cells are attached for budding colonies in (B) and after separation in (C). (See Section 4.2.2 for how we define connectivity.) (A) We observe a statistically significant difference in colony connectivity at 12 h ($p = 3.602 \times 10^{-04}$), 18 h ($p = 8.921 \times 10^{-29}$), 24 h ($p = 1.094 \times 10^{-79}$) and 28 h ($p = 3.389 \times 10^{-110}$). (B) We observe a rapid decrease in connectivity for non-budding colonies between 12–18, 18–24, and 24–28 h. This decrease leads to a statistically significant difference between budding and non-budding colonies at 12 h ($p = 6.834 \times 10^{-05}$), 18 h ($p = 4.670 \times 10^{-40}$), 24 h ($p = 1.050 \times 10^{-92}$) and 28 h ($p = 2.658 \times 10^{-122}$). (C) We observe a statistically significant difference in connectivity at 18 h ($p = 1.144 \times 10^{-15}$), 24 h ($p = 1.888 \times 10^{-58}$) and 28 h ($p = 2.140 \times 10^{-83}$). (p -values for connectivity were computed using independent t -tests. p -value annotation is as follows. *: $1.0 \times 10^{-2} p \leq 5.0 \times 10^{-2}$, **: $1.0 \times 10^{-3} p \leq 1.0 \times 10^{-2}$, ***: $1.0 \times 10^{-4} p \leq 1.0 \times 10^{-3}$, ****: $p \leq 1.0 \times 10^{-4}$); (D) Kaplan-Meier survival curves for the edge connecting mother-daughter cell pairs in G_5 for budding (red) and non-budding (blue) colonies. The y -axis is the probability that a given mother-daughter edge will remain in G_5 for longer than t hours after separation, where time is on the x -axis. We observe that the survival curves are different between the two groups ($p = 1.314 \times 10^{-75}$) indicating that the probability that a mother-daughter edge remains in the spatial graph for longer than t hours is greater for budding colonies. (The p -value comparing survival curves was calculated using a log-rank test as described in Section 4.3. See Section 2.2.3 for details.)

As above, we analyzed connectivity between mother and daughter pairs in two distinct phases: when they are attached for budding cell division (budded cells, Figure 9B) and after separation (un-budded cells, Figure 9C). We observe that, as in nutrient-rich growth, the connectivity between mother and daughter cells in both phases was higher for budding cell division, and that this difference

in connectivity between division types increases in time. However, we note that the connectivity for un-budded cells was slightly higher at the 24 h time point in the nutrient-rich growth condition (compare Figure 5C with Figure 9C).

We believe the explanation for both the overall higher colony connectivity in nutrient-limited growth (panel A) and the decreased connectivity for un-budded cells (panel C) is due to the impact of nutrient availability on the cell cycle and position of newly born cells. More specifically, the extended cell cycle induced by nutrient limitation (i.e. cells stay in the budding phase longer) creates an overall higher colony connectivity because daughter cells stay attached longer. In addition, the age structure of the colony, where newly born cells are more likely to be at the colony perimeter, means that these newly born cells have more space to move away from their mother when they detach.

To better understand the impact of nutrient limitation and budding on the duration of the mother-daughter edges in G_S , we generated Kaplan-Meier survival curves (Figure 9D). We observed that the probability the mother-daughter edge stays in G_S for longer than t hours after separation is higher in budding colonies. In addition, the restricted mean survival time for mother-daughter edges in budding colonies was 67 min compared to 52 min for non-budding colonies. However, as expected by our explanation for Figure 9B,C, we observe the median duration of a mother-daughter edge in G_S is shorter when compared to the nutrient-rich condition.

2.2.4. Nutrient Limitation Further Promotes Subcolony Connectivity

Next we investigated the impact of nutrient limitation together with budding division on subcolony organization and connectivity. To do this, we first analyzed the number of connected components between budding and non-budding colonies in nutrient-limited conditions. We find that nutrient-limited growth results in a significant decrease in the number of connected components for both budding and non-budding colonies compared to nutrient-rich growth. (Compare Figure 6A to Figure 10A.) However, we also observe that the number of connected components for each of the first five subcolonies is significantly lower in budding colonies (Figure 10A). In addition, we see that the average time elapsed from creation of a given subcolony until it splits into more than 5 connected components is significantly lower in non-budding colonies (Figure 10B). These results not only reveal that nutrient limitation has a large impact on subcolony structure and connectivity, but also confirm that budding division maintains its role in promoting subcolony connectivity under nutrient limitation.

To further investigate the impact of nutrient limitation and budding division together on subcolony structure and connectivity we considered the number of cells contained in small connected components (i.e., less than 10 cells). We find that nutrient limitation results in a large decrease in the total number of cells belonging to a small connected component (i.e., less than 10 cells) for both budding and non-budding colonies at the 24 h time point (compare Figure 6C with Figure 10C). This further highlights the strong impact of nutrient limitation on subcolony structure. In addition, we observe a significant difference in the number of cells in a small connected component between budding and non-budding colonies at the 18, 24, and 28 h time points. Moreover, we find that the survival curves for the time elapsed from creation of a subcolony to when it splits into more than 5 components are different between budding and non-budding colonies (Figure 6D), indicating that the probability that a given subcolony remains connected (i.e., less than 5 connected components) for longer than t hours is greater for budding colonies. Similarly as before, we considered this a separate event for each of the first 5 subcolonies and each of our 50 simulations. These results further support our observation that budding division acts as a mechanism increasing spatial adjacency within subcolonies in both nutrient-rich and nutrient-limited conditions.

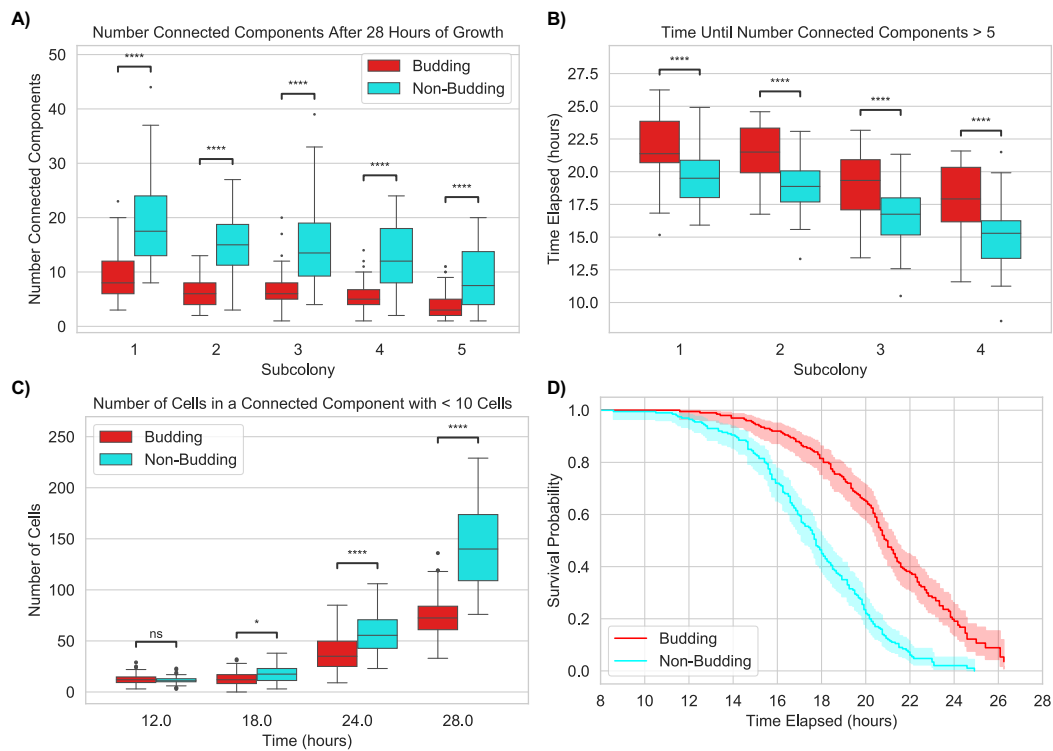


Figure 10. Subcolony Structure and Organization in Nutrient-Limited Colonies. **(A)** Comparison of the number of connected components for the first five subcolonies between budding (red) and non-budding (blue) colonies at the 28 h time point. We observe a statistically significant difference in the number of connected components for subcolony 1 ($p = 3.39 \times 10^{-10}$), subcolony 2 ($p = 4.454 \times 10^{-17}$), subcolony 3 ($p = 8.537 \times 10^{-11}$), subcolony 4 ($p = 2.884 \times 10^{-11}$) and subcolony 5 ($p = 3.783 \times 10^{-06}$). **(B)** Comparison of time until each of the first five subcolonies splits into 5 connected components. We observe a statistically significant difference between budding (red) and non-budding (blue) colonies for subcolony 1 ($p = 8.967 \times 10^{-05}$), subcolony 2 ($p = 6.246 \times 10^{-08}$), subcolony 3 ($p = 8.636 \times 10^{-05}$), and subcolony 4 ($p = 9.154 \times 10^{-06}$). **(C)** Comparison of the number of cells in a connected component with less than 10 cells. Note that nutrient-limited growth results in a large decrease in the total number of cells in small components at the 24 h time point compared to nutrient-rich growth. However, we still observe a statistically significant difference between budding (red) and non-budding (blue) colonies at 18 h ($p = 3.537 \times 10^{-02}$), 24 h ($p = 9.040 \times 10^{-07}$), and 28 h ($p = 5.410 \times 10^{-18}$). **(D)** Kaplan-Meier survival curves for the length of time a subcolony is made up of less than 5 connected components for budding (red) and non-budding (blue) colonies. The y -axis is the probability that a subcolony consists of less than 5 connected components for longer than t hours, where time is on the x -axis. We observed that the survival curves are different between the budding and non-budding colonies ($p = 2.428 \times 10^{-23}$) indicating that the probability that a given subcolony remains connected (i.e., less than 5 connected components) for longer than t hours is greater for budding colonies. (The p -value comparing survival curves was calculated using a log-rank test as described in Section 4.3. In addition, 95% confidence intervals for the survival function are shown. See Section 2.2.4 for details.)

2.2.5. Nutrient Limitation Changes Global Colony Organization by Driving Variation in Subcolony Sizes

Results from our previous metrics provide compelling evidence that nutrient limitation has a large impact on spatial organization of growing yeast colonies. However, the strongest demonstration of the impact of nutrient-limited growth on morphological properties of growing yeast colonies is its effect on emergent patterns of subcolony structure and organization for which we do not yet have an explicit quantitative metric. Specifically, simulations of nutrient-limited colonies result in the appearance of

subcolonies that grow in a “sector-like” formation (compare Figure 11 (top and middle) with Figure 2 (middle and bottom)). Namely, subcolony boundaries in nutrient-limited simulations are more linear. This is especially visible in the last time point at 28 h.

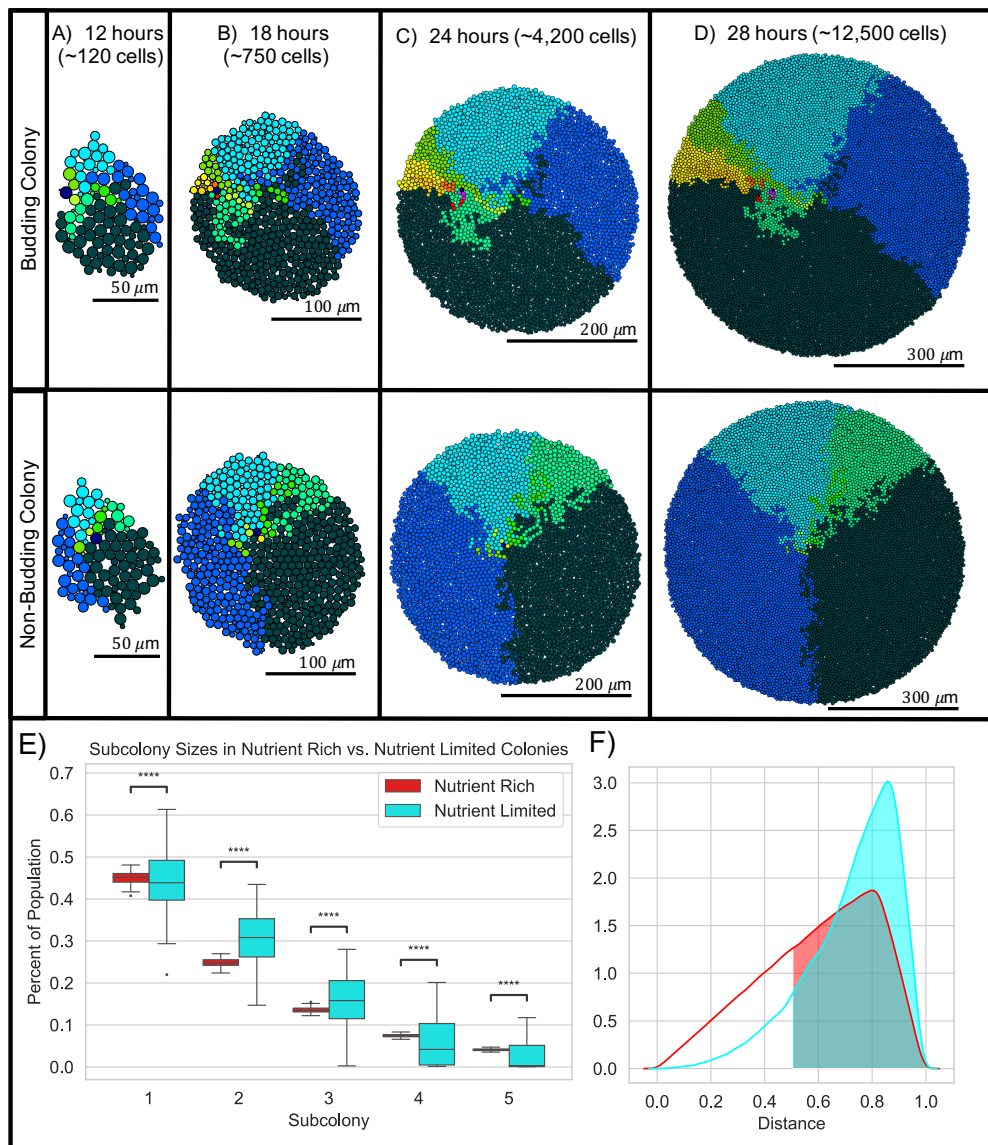


Figure 11. Nutrient Limitation Drives Spatial Organization of Cells. We compared growth and overall spatial organization between four different types of colonies (budding/non-budding, nutrient-rich/nutrient-limited). Cells in colonies are colored according to the unique subcolony each cell belongs to: Subcolony 1 (dark green), Subcolony 2 (blue), Subcolony 3 (cyan), Subcolony 4 (teal), Subcolony 5 (light green), Subcolony 6 (yellow-green), Subcolony 7 (yellow), Subcolony 8 (gold), Subcolony 9 (orange), Subcolony 10 (red), Subcolony 11 (magenta), Subcolony 12 (purple) and Subcolony 13 (pink). Typical simulation output from budding and non-budding colonies grown in nutrient-limited conditions: 12 hours (A), 18 hours (B), 24 hours (C), 28 hours (D). (E) Nutrient limitation results in more variation in the percentage of the population contained in each subcolony (Subcolony 1 ($p = 2.779 \times 10^{-20}$), Subcolony 2 ($p = 6.143 \times 10^{-25}$), Subcolony 3 ($p = 4.636 \times 10^{-23}$), Subcolony 4 ($p = 6.574 \times 10^{-32}$), and Subcolony 5 ($p = 2.985 \times 10^{-09}$)). (p -values were calculated using the Levene test for equal variances. p -value annotation is as follows. *: $1.0 \times 10^{-2} p \leq 5.0 \times 10^{-2}$, **: $1.0 \times 10^{-3} p \leq 1.0 \times 10^{-2}$, ***: $1.0 \times 10^{-4} p \leq 1.0 \times 10^{-3}$, ****: $p \leq 1.0 \times 10^{-4}$.) (F) Birth Location of cells born within the last hour of colony growth changes significantly between nutrient-rich (red) and nutrient-limited (cyan) conditions ($p < 1.0 \times 10^{-32}$). (p -value was calculated using the Kolmogorov-Smirnov statistic in python. See Section 2.2.5 for details.)

In addition, unlike colonies grown in nutrient-rich conditions, colonies grown in nutrient-limited conditions have highly variable subcolony sizes as a percentage of the colony. For example, consider the different sizes of the first subcolony (dark green) in both the top and middle row of Figure 11. At 28 h, the first subcolony in the top row appears to consist of close to half of the total population. At the same time point, the first subcolony in the middle row makes up only a third of the total population. Moreover, in the top row, the first (dark green) and second (dark blue) subcolonies are noticeably different sizes, while in the middle row they are almost exactly the same size. Finally, we note that the colony in the top row (budding) has 13 subcolonies whereas the colony in the middle row (non-budding) has only 7. This is due to variation in the number of daughters produced by the founder cell. Interestingly, we found the variation observed in subcolony sizes did not differ between budding and non-budding conditions but was a property purely driven by nutrient limitation.

To investigate the variation in subcolony sizes between nutrient-rich and nutrient-limited growth, we computed the final percentage of the entire colony contained in each subcolony for nutrient-rich (24 h) and nutrient-limited (28 h) growth. As shown in Figure 11E, the nutrient-limited colonies have significantly higher variation. We conjecture that this difference in subcolony final composition is due to biases induced by global changes in age and birth structure. To test this conjecture we compared the empirical probability density functions for normalized birth location of cells born in the last hour of growth between nutrient-rich and nutrient-limited colonies (Figure 11F). We found that the two empirical distributions are significantly different, indicating that cells in nutrient-limited colonies are more likely to be born at the edge of the colony. These results support our observation that budding division impacts local organization of growing yeast colonies while nutrient-limited growth changes global patterns of colony organization. To our knowledge, this difference in final subcolony variation in nutrient-limited growth has not been explicitly explored for budding division or yeast. Moreover, we note that since this difference is due to nutrient-limited conditions, this variation would not hold for yeast colonies grown in liquid culture.

3. Discussion

As described in the introduction, morphological patterns in microbial colonies arise due to processes at different scales (Figure 1). In this paper, we developed a 2D ABM and used it to quantify the biophysical impact of budding cell division on the overall shape, size and spatial organization of growing yeast colonies. The novelty of our approach is that we explicitly model the mechanical interactions that arise due to budding cell division. An additional novelty lies in the metrics we developed to quantify spatial organization of cells within the colony. Moreover, results from these metrics reveal the impact of budding division and nutrient limitation on patterns of displacement and spatial rearrangement of cells leading to emergent local and global morphological properties of growing yeast colonies.

In Section 2.1, our findings reveal that budding division does not impact global, large-scale structures of growing yeast colonies (Figure 3B,C), or the birth location of cells within the colony (Figure 4C,D). However, we find that budding division substantially impacts local organization of cells including enforcing a smaller physical distance between mother and daughter cells even after separation. We believe this physical closeness is the consequence of two forces. First, the budding division process means mother and daughter cells are forced to be connected for a longer period of time than in non-budding colonies. Second, this prolonged connection means that when the mother and daughter cells do separate, the local environment is more likely to be “crowded” and thus mother-daughter cell pairs are more likely to remain close. This overall closeness between mother and daughter cells results in greater connectivity in the colony in terms of a larger proportion of mother-daughter edges in G_5 (i.e., the colony connectivity metric, Figure 5) as well as subcolonies that consist of smaller numbers of connected components.

In Section 2.2, our findings reveal that nutrient limitation plays a significant role in directing global, large-scale colony organization. Our simple model of nutrient limitation produced colonies

that grew more slowly (average doubling time of ~ 123 min compared to ~ 105 min for nutrient-rich colonies) (Figure 11A–D). In addition, cells in nutrient-limited colonies were much more likely to be born near the edge of the colony, where nutrients are more readily available, than near the middle, where nutrients are highly depleted (Figure 11F). Moreover, since lack of nutrients slows down cell cycle progression, most actively dividing cells are near the boundary of the colony. As such, our model captures emergent patterns of colony organization due to changes in local cell-cell interaction dynamics caused by rapid expansion and spatial rearrangement of newly born cells at the colony boundary. An interesting extension of our model would be to compare simulation results with our simple model of nutrient limitation to simulation results representing a nutrient field that changes in time due to diffusion and consumption by live cells.

Our results also reveal that together, budding and nutrient-limited growth facilitate subcolony connectivity. We observe that nutrient-limited growth in our simulations results in better defined and more contiguous subcolonies than in the nutrient-rich case (Figure 11A–D). This is likely due to the effects of nutrient limitation on the cell cycle for densely packed regions of the colony. Furthermore, the nutrient limitation condition creates high variance in the final number of cells that will be in each subcolony at a particular time (Figure 11E). We believe this variation is caused by different patterns of movement of the founder cell. Namely, if the founder cell is moved to areas of high nutrient availability due to interactions with neighboring cells, it can produce more offspring. Otherwise, if cell-cell interactions cause it to remain stationary in low-nutrient regions, its cell cycle progression will be slowed resulting in fewer total offspring. These observations further support the idea that nutrient-limited growth together with budding division result in colonies with the most well-defined subcolony shapes. We hypothesize that these contiguous subcolonies are precisely the discernible sectors observed in experimental yeast colonies. As such, our mathematical framework will provide valuable insight for generating hypotheses on sectoring behavior that can be compared to experimental studies. This variation in subcolony size from nutrient limitation will have a different impact for cells grown on a plate (i.e., physical media) compared to those in liquid culture (where cells are in a well-mixed liquid environment) and our work identifies population structure as a novel and unappreciated difference in these two common experimental conditions. As such, changes in population structure are a new lens through which experiments in these conditions can be compared. In addition to its impact on local spatial organization and subcolony structure, resource-driven structuring in microbial groups has been linked to colony fitness and survival [8,29]. Our results suggest that nutrient-rich colonies have less structure and therefore allow a greater number of lineages to be maintained as the colony expands. This is in contrast to our simulations of nutrient-limited colonies where the number and sizes of subcolonies undergoes a lot more variation. An interesting avenue of further study would be to run simulations for a longer amount of time and assess how nutrient limitation impacts overall colony fitness and survival other than the overall slower growth we describe in our results.

We note that there are many cellular processes that our model did not explicitly consider. First, we did not include cell rotational forces in our model. Based on results in this paper, biophysical properties of attached mother-daughter cell pairs play a role in local organizational properties of colonies. Thus, we believe extending our model to include rotational forces and capture more detailed geometry of attached mother-daughter cell pairs may further impact local organization dynamics. In addition, in nutrient-limited conditions, cells may enter a state of quiescence where they choose not to enter the G1 phase of the cell cycle [54]. Although we did not directly include quiescence as a state in our model, cells in our simulations do attain an effective “quiescence” state as they stop growing and creating new buds due to limits on their cell cycle progression. Third, our model does not include cell death. Although cell death is definitely a contributor to colony structure, specifically the 3D structure of colonies where the middle section is nutrient-starved, because the average lifetime of yeast cells exceeds the time-scale of our simulations [55,56], the impact of cell death on the organization phenomena we observe is negligible.

Finally, we have included only one type of budding behavior. Yeast are capable of multiple budding strategies. For example, we do not consider multiple cell mating types and only consider diploid cells. While diploid yeast cells primarily divide in a bipolar budding pattern [57], haploid cells can bud in an axial pattern [27] and have been shown to divide faster than diploid cells [58]. If we only considered diploid cells with no variance in the location of the new birth scar, all cells would appear co-linear to each other. However this extreme case is unlikely to occur within large diploid colonies [27]. We model new budding sites in a manner similar to the implementation by Wang et al. [42], but we consider only daughter cells to be limited to bipolar cell division. In addition, we assume that a mother cell has at most one daughter cell attached, but this is not guaranteed for all strains [59]. Furthermore, we also neglect environmental factors in influencing budding strategies. While cells in larger yeast colonies have been shown to exhibit pseudohyphal growth through switches in budding strategies under nutrient-limited conditions [32,60,61], it was reported by Binder et al. [60] that colony expansion appears to evolve non-uniformly after approximately 100 h. Because this far exceeds the time scales of the colonies we produced, we believe this effect to be negligible. However, we conjecture that for large colonies, pseudohyphal growth under nutrient-limited conditions will induce rapid changes in colony organization near the colony periphery.

Indeed several agent-based modeling frameworks have been developed to study the factors impacting yeast colony growth. Jönsson et al. developed a similar center-based model to study the impact of biophysical factors and growth inhibition by neighboring cells on colony expanse and sparsity [41]. Their results show that cell-growth inhibition by neighboring cells and bipolar division patterns are the most significant factors impacting colony sparsity where they used colony sparsity as a measure of exploratory behavior of the colony. However, their results focused on global shape and size of colonies instead of spatial organization of cells, and they did not consider colonies larger than several hundred cells. Wang et al. developed a center-based model to study the impact of budding patterns, mating type switches, cell death and nutrient limitation on yeast colony growth [42]. Consistent with Jönsson et al., they found that bipolar budding patterns improve colony development under nutrient limitation. In addition, they found that axial budding patterns enhance mating probability during early stages of colony growth and suggest that the frequency of mating type switch might control the trade-off between diploidization and inbreeding. Interestingly, they showed that colony expansion does not depend on the overall age of the colony. They hypothesize this is due to the fact that young cells contribute most to colony expansion which is consistent with our results. One important difference between our model and the model presented by Wang et al., is that our model explicitly includes the process of a bud growing on the mother cell. The model by Wang et al. skips the growing process and introduces new daughter cells after they have detached from the mother cell and are a more substantial size. In addition, their study focused on characterizing heterogeneity of cell types in the colony and overall shape and size of the colony and they did not analyze the impact of spatial organization of cells. Since their model does incorporate many of the important factors we discussed above as possibly having an impact on spatial organization and structure of the colony, we believe an interesting avenue for future work would be to extend our model to include the same factors they considered and investigate how the addition of the budding process changes the resulting outcomes discussed in their paper.

Many questions remain in investigating the structure of growing yeast colonies, and our model may be easily generalized to include them. In particular, we plan to extend our model by including intracellular protein dynamics to more directly study prion sectors in yeast. Despite many years of biomedical research and our detailed understanding of protein aggregation dynamics on the molecular scale, our ability to mechanistically link protein aggregation processes to their disease phenotypes at the colony level is severely lacking, especially during transitions between prion states [62–65]. For example, recent studies have demonstrated that a single colony can exhibit multiple phenotypes resulting from a change in aggregation dynamics between neighboring cells [3]. Our results in Section 2.2.4 demonstrate that nutrient limitation and budding together have a large

impact on emergent patterns of sector-like regions in growing yeast colonies. Moreover, an important insight of our work is the large variation in subcolony sizes that arises due to nutrient-limited growth. As a consequence of this result, we can better understand that the size of a subcolony sector is not directly correlated to its birth order. Thus, quantitative information connecting spatial information of sectoring patterns with molecular level dynamics is required. What is missing is a detailed and mechanistic computational model of sectoring phenomena which can then be coupled with an informatics look at the sectors in experiments. Methods and tools for counting different colonies have been developed which may aid in detecting phenotype sectors through finding connected groups of cells [66–68]. While there are resources that quantify sectoring in microbial colonies [5,8], to our knowledge no other studies specifically quantify the causes of phenotype sectoring in yeast colonies. Our modeling framework can be readily extended to a multi-scale system to address phenotype sectoring in yeast through the incorporation of prion dynamics as a subcellular process (Figure 1). This offers the opportunity to make more meaningful comparisons between data and models and to infer, predict, and eliminate hypotheses on the characteristics of the sectoring patterns.

In this study we proposed a 2D model of yeast colony growth, where directional forces along the Z-axis are neglected. In reality, yeast colonies are three-dimensional (3D). Thus, there may be some important factors our model does not consider. For example, in 3D, high agar concentrations have been shown to influence formation of complex structures such as the vertical growth of stalk-like structures in yeast colonies [69]. In this scenario, complete contact with the substrate is not possible for all cells further impacting nutrient availability. Experimental evidence also shows that microbial colonies do not grow outward in a strictly radial direction due to varying agar concentrations [70] and de-activation of the FLO11 gene which reduces adhesion of the cells to the plate surface [71]. Thus, while cell dependency on nutrients is more complicated to model in 3D, these results suggest it will remain an important factor driving variances in colony morphology. Moreover, we hypothesize that 3D configuration may further promote local spatial organization, sectoring patterns and ordered structure of the colony. In our model, we study the formation of sector-like regions in the context of subcolonies. Under nutrient limitation, our model shows that subcolony sectors become more well-defined and begin near the location of the founder cell. However in 3D, different technologies used to capture and analyze sectoring phenomena may be limited to the colony surface. The capability of *in silico* experiments creates the advantage of allowing for more detailed analyses of sectoring phenomena where existing scientific tools and technologies may not provide sufficient information.

4. Materials And Methods

In this section, we develop the 2D, off-lattice, center-based model we use to simulate the growth of *S. cerevisiae* colonies (Figure 12) as well as describe the metrics we use to analyze simulation output. In the model, each cell is represented by an elastic sphere that moves, grows, buds and divides according to biophysical and cell-kinetic model parameters estimated from experiments (Table 1). We simulate artificial yeast colonies under two different division formulations (budding and non-budding) and growth conditions (nutrient-rich and nutrient-limited).

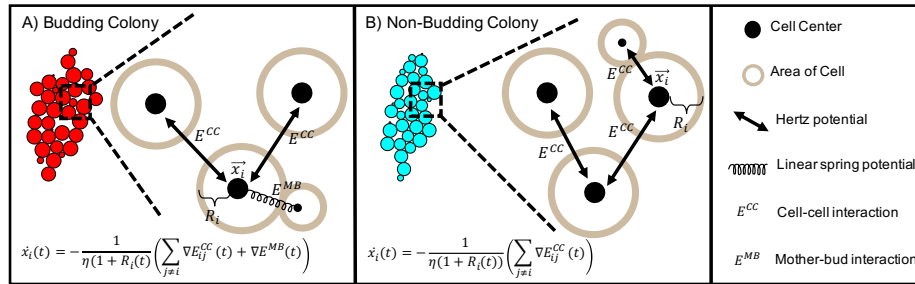


Figure 12. Biophysical Model of Cell-Cell Interactions. We simulate budding (A) and non-budding (B) colonies using a 2D center-based modeling approach where cells interact through different potentials. (A) For budding colonies, the mechanical interactions of all cell pairs (E^{CC}) are governed by a combination of repulsive and attractive interactions using a modified Hertz-model described in Equation (1). We use a linear spring to model the additional adhesive force between mother cells and new daughter cells during the budding phase (E^{MB}) as in Equation (4); (B) For non-budding colonies, the mechanical interactions are similar to that of cells in budding colonies except that the adhesive force between mother cells and new daughter cells during the budding phase (E^{MB}) is neglected (see Section 4.1.1 for details).

4.1. Computational Model

Below we develop our computational ABM for studying yeast colony growth and structure. In simulations of budding colonies we explicitly model the mechanical interactions during budding cell division by modeling the daughter cell as a growing circle attached to the mother cell with a stiff spring (Figure 12A and Figure 14). In contrast, in simulations of non-budding colonies we treat mechanical interactions of mother-bud pairs as identical to other cell-cell pairings (Figure 12B).

4.1.1. Cell-Cell Interaction and Spatial Arrangement Of Cells

We assume the resting shape of individual yeast cells is circular, and track the size and location of cell i at time t by its radius $R_i(t)$ and center $\vec{x}_i(t) = (x_i(t), y_i(t))$ (Figure 12). We track the total number of cells at time t , $N(t)$, and index cells by their birth order $i \in \{1, 2, \dots, N(t)\}$. Since all cells are of the same type, the mass of each cell, $m_i(t)$, is proportional to the area of each cell with the same constant. Yeast cells interact through different potentials that we use to represent biologically-relevant processes seen in experiments (Figure 12). For example, yeast cells in physical contact form adhesive bonds that result in an attractive force [41,42,44,72,73]. However, due to the incompressibility of their cell wall, yeast cells also resist compression from neighboring cells with a repulsive force [41,42,44,74,75]. We represent the combination of repulsive and attractive interactions between cells using a modified Hertz-model, as has been previously done [48,51,76,77], where the potential $E_{ij}^{CC}(t)$ between two cells i and j is given by:

$$E_{ij}^{CC}(t) = \frac{(R_i(t) + R_j(t) - d_{ij}(t))^{5/2}}{5\tilde{E}_{ij}} \sqrt{\frac{R_i(t)R_j(t)}{R_i(t) + R_j(t)}} + E_{ij}^{adh}(t). \quad (1)$$

The first term of Equation (1) depicts the repulsive interaction and $d_{ij}(t) = \|\vec{x}_i(t) - \vec{x}_j(t)\|$. In this equation $\tilde{E}_{ij}(t)$ is defined by:

$$\tilde{E}_{ij} = \frac{3}{2} \left(\frac{1 - \sigma^2}{E} \right) \quad (2)$$

where E and σ are the Young's moduli and Poisson ratios of cells, respectively. The second term of Equation (1) models the adhesive interaction between cells and is given by:

$$E_{ij}^{adh}(t) = \phi W_s A_{ij}(t) \tag{3}$$

where ϕ is the density of surface adhesion molecules in the contact area, W_s is the single bond bind energy and $A_{ij}(t) = (R_i(t) + R_j(t)) \times 0.5$ is the contact area between cells i and j .

In simulations of non-budding colonies, the mechanical interactions of all cell pairs are given by Equation (1). However, in simulations of budding colonies, we explicitly model an additional force between mother cells and new daughter cells during the budding phase (Section 4.1.2, Figure 12A and Figure 14). To do this, we represent the adhesive interaction caused by attachment of the new daughter cell to its mother using a linear spring potential given by:

$$E_{mb}^{MB}(t) = K_{bud} (d_{mb}(t) - (R_m(t) + R_b(t)))^2 \tag{4}$$

where $d_{mb}(t) = \|\vec{x}_m(t) - \vec{x}_b(t)\|$, $R_m(t)$ is the radius of the mother cell at time t , $R_b(t)$ is the radius of daughter cell at time t and K_{bud} is a spring constant chosen large enough to ensure that the new daughter cell b remains attached to its mother for the duration of the budding phase and is not pushed away due to forces from other neighboring cells.

In addition, we assume that cells are in an overdamped regime so that inertial forces acting on the cells are neglected [78–80]. This leads to the following equation of motion describing the movement of an individual yeast cell i in a budding colony:

$$(\eta(1 + R_i(t)/2)) \dot{x}_i(t) = \begin{cases} - \left(\sum_{i \neq j} \nabla E_{ij}^{CC}(t) + \nabla E_{ij}^{MB}(t) \right) & i \text{ is a bud} \\ - \left(\sum_{i \neq j} \nabla E_{ij}^{CC}(t) + \nabla E_{ij}^{MB}(t) \right) & i \text{ is a mother with an attached bud} \\ - \left(\sum_{i \neq j} \nabla E_{ij}^{CC}(t) \right) & \text{else} \end{cases} \tag{5}$$

where j indexes the other cells in the colony at time t and η is the damping coefficient that represents viscosity of the growth media and is scaled by $(1 + R_i(t)/2)$. The equation of motion describing the movement of all cells in a non-budding colony simplifies to only the third case in Equation (5).

The equation of motion of a cell is discretized in time using the forward Euler method, and the position $\vec{x}_i(t)$ of cell i at time t is given by:

$$\vec{x}_i(t + \Delta t) = \vec{x}_i(t) - \left(\sum_{i \neq j} \nabla E_{ij}^{CC}(t) + \nabla E_{ij}^{MB}(t) \right) \frac{\Delta t}{\eta(1 + R_i(t)/2)} \tag{6}$$

where Δt is the time step size. The same discretization technique is used for all cells in each simulation.

4.1.2. Budding Cell Division

S. cerevisiae cells undergo budding cell division [26,28]. During this process, one large mother-daughter cell pair is formed by the appearance of a bud on the mother. The bud (or new daughter) remains attached while it gradually grows into a larger cell (Figure 14). At the time of division, the mother cell and new daughter become physically separated resulting in two unevenly sized cells. After division, a bud scar is left on the surface of mother cell at the location where the new daughter was formed, and no subsequent buds can be formed at that site (Figure 13). Similarly, a birth scar is left on the surface of the new daughter cell.

The location of the bud on the surface of the mother cell can be chosen according to two distinct patterns, axial or bipolar [24–26,41,42]. In our model we follow Reference [42] and model budding cell division with the the following pattern: mother cells are equally likely to choose a new bud location adjacent to or opposite from the previous bud location, and daughter cells always bud

opposite to their birth scar (Figure 13). To ensure no bud/birth scars are used twice, we keep track of all previous bud/birth sites for every cell. If the next choice for a bud site falls on a previously used location we adjust the location of the new bud site by increments of 10° in either the clockwise (probability = 0.5) or counterclockwise (probability = 0.5) direction until we arrive at a location with no previous bud/birth scar (Figure 13 (Left)). The budding location of the founder cell’s first daughter is chosen randomly and uniformly along its boundary.

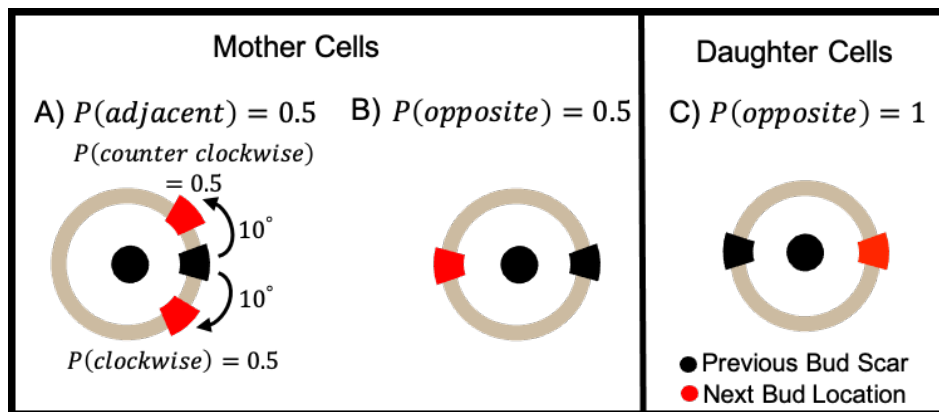


Figure 13. Selecting a Bud Site. The choice of the next bud location for a cell depends on whether it is a mother cell (left) or a new daughter cell (right). (Left) For mother cells, the next bud location will be chosen either adjacent to the previous bud scar with probability 0.5 (A) or opposite to the previous bud scar with probability 0.5 (B). In the case when the location of the new bud site overlaps with a previous bud site (A), we adjust the location of the new bud site by increments of 10° in either the clockwise (probability 0.5) or counterclockwise (probability 0.5) direction until we arrive at a location with no previous bud scar. (Right) For new daughter cells the next bud location (red) is chosen opposite to the previous birth scar (black) with probability 1 (C). New daughter cells that have successfully completed a full cell cycle are considered mother cells for the remainder of the simulation. (See Section 4.1.3.)

4.1.3. Cell Growth and Cell Cycle Length

We follow the standard model of eukaryotic cell division and consider the cell cycle to have two distinct growth phases: G1 and G2. At the time of separation, mother and new daughter cells are unequal in size. Thus, new daughter cells undergo an extended G1 phase in order to grow to a mature adult size before producing their own bud [81]. (Figure 14.) In our model, the average cell cycle length for mother cells is ≈ 90 min (~ 15 min in G1 and ~ 75 min in G2) and the average cell cycle length for new daughters cells is ≈ 120 min (~ 75 min for the “Budding” phase while attached to their mother and ~ 45 min growing on their own). To depict more realistic cell cycle dynamics, we introduce an element of stochasticity to the cell division times.

The variable **Cell Progress** ($CP \in [0, 1]$) is used to track the progress of individual cells through the G1 and G2 phases. In our model, the progress of cell i at time t is given by:

$$CP_i(t) = CP_i(t - \Delta t) + CI_i \times \Delta t \tag{7}$$

where $CI_i = (G1_i + G2_i)^{-1}$. The length of $G2_i$ is computed once for all cells:

$$G2_i = (1 + \mathbf{U}[-0.1, 0.1]) G2_{avg}.$$

(In the previous expression $\mathbf{U}[-0.1, 0.1]$ is a uniformly distributed random variable on the interval $[-0.1, 0.1]$.) To represent the longer G1 phase of daughter cells, the length of $G1_i$ is assigned once upon creation of a new bud

$$G1_{i_{new\ daughter}} = (1 + \mathbf{U}[-0.1, 0.1]) G1_{avg_{daughter}}$$

and then updated once the new daughter cell completes its first G1 phase and forms a bud of its own

$$G1_{i_{mother}} = (1 + \mathbf{U}[-0.1, 0.1]) G1_{avg_{mother}}.$$

In the G1 phase, mother cells have already reached their adult size, so the G1 phase is simply a waiting time until entering the G2 phase where they form a bud (or new daughter). Every new bud is initiated with a radius of size $0\mu\text{m}$ and grows for ≈ 75 minutes while attached to its mother. (This 75 minutes of attachment accounts for the entire G2 phase of the mother and make up the first part of the G1 phase for the daughter.) After this phase, the mother and bud are physically separated resulting in a new daughter cell. At separation, the mother cell enters the G1 phase, and the new daughter cell stays in its G1 phase and continues to grow for ≈ 45 minutes until it reaches its adult radius size (Figure 14). At this time, the daughter cell transitions into a mother cell and begins to produce its first bud.

The adult size, corresponding to a maximum radius R_{max} , is assigned to each cell upon creation and set to

$$R_{i,max} = (1 + \mathbf{U}[-0.1, 0.1]) R_{avg}.$$

The radius of cell i at time t is given by:

$$R_i(t) = \begin{cases} R_i(t - \Delta t) + \frac{R_{i,max}}{G1_i} \times \Delta t & R_i(t) \leq R_{i,max} \\ R_{i,max} & \text{else.} \end{cases} \quad (8)$$

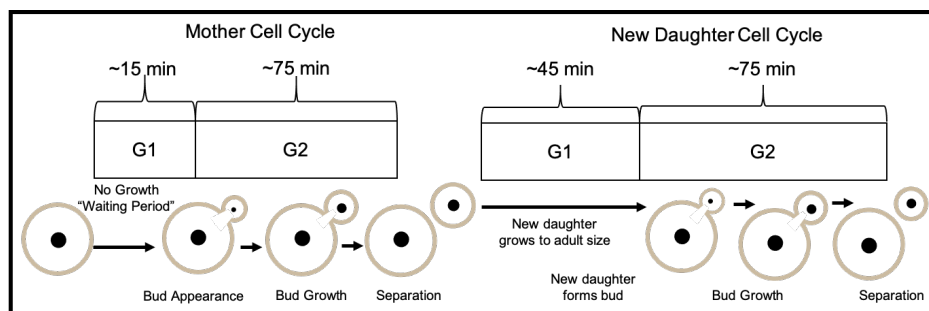


Figure 14. Cell Cycle Length. (Left): The G1 phase for mother cells is approximately 15 min. Since mother cells have already reached their adult size, the G1 phase serves as a waiting period before the mother cell enters G2 and forms a bud. When the mother cell enters G2, the new daughter cell forms as a bud and stays attached for ~ 75 min as it grows. After ~ 75 min, the mother and new daughter physically separate resulting in two unevenly sized cells. At this time, the mother cell enters G1 and begins a new cell cycle. (Right): The new daughter cell continues to grow until it reaches its adult size (~ 45 min) and forms its own bud. Under nutrient-limited conditions, the length of the G1 and G2 phases are increased for both mother and daughter cells (see Section 4.1.4 for details).

4.1.4. Nutrient-Limited Growth

Until now, we assumed that the environment cells were in contained an inexhaustible nutrient supply and cell maturation and division occurs at the same rate no matter how many cells were present. We now revisit this assumption by modeling the growth of individual yeast cells as dependent on a local nutrient supply. That is, a depletion in nutrient concentration slows down individual cell growth by prolonging the cell cycle length. Previous studies have incorporated the effect of enzyme and/or nutrient concentration on individual cell behaviors in ABM models of microbial colony growth [8,29,42,48–53]. The majority of these studies use reaction-diffusion equations that include the uptake of growth substrate by each cell to compute spatial gradients of enzyme or nutrient concentration. For simplicity, we consider each region of our simulation domain to have a maximal

possible biomass (i.e. carrying capacity). We divide the simulation domain into smaller subdomains and adjust the cell cycle progression $CP(t)$ for cells in each subdomain j at time t as follows.

First, for each cell i we track the subdomain the cell is in denoted $D_i(t)$ and compute the total mass of cells in each subdomain j where $m_i(t) = \pi R_i(t)^2$:

$$M_j(t) = \begin{cases} \frac{\sum_{i=1}^{N(t)} m_i(t) \mathbb{I}_j(D_i(t))}{M_{j,\max}}, & \text{if } \sum_{i=1}^{N(t)} m_i(t) \mathbb{I}_j(D_i(t)) \leq M_{j,\max} \\ 1 & \text{else} \end{cases} \quad (9)$$

where \mathbb{I}_j is an indicator variable that equals 1 if $D_i(t) = j$ and 0 otherwise. Note that in practice $M_{j,\max}$ is chosen large enough that $\frac{M_j(t)}{M_{j,\max}}$ is always less than 1.

Next, we define a growth-rate adjustment factor for each subdomain that is initialized to 1 at the beginning of simulations and decreases in time according to the following equation:

$$GR_{\text{adjust}}(t) = \begin{cases} GR_{\text{adjust}}(t - \Delta t, j) - rM_j(t)\Delta t, & \text{if } \frac{GR_{\text{adjust}}(t - \Delta t, j)}{\Delta t} \geq -rM_j(t) \\ 0 & \text{else} \end{cases} \quad (10)$$

where $M_{j,\max}$ is the carrying capacity for the j -th subdomain and r is the per capita rate of decrease of GR_{adjust} . We then re-scale the cell cycle increment:

$$\widetilde{CI}_i(t) = CI_i(t) \times GR_{\text{adjust}}(t, D_i(t)) \quad (11)$$

and thus the cell progression in nutrient-limited growth becomes

$$CP_i(t) = CP_i(t - \Delta t) + \widetilde{CI}_i(t) \times \Delta t. \quad (12)$$

As the colony grows, cells move, new cells are born and cells are displaced into new subdomains. To account for this we calculate the growth rate adjustment factor for each subdomain at each timestep, and use it to update $\widetilde{CI}_i(t)$ for each cell according to the unique subdomain it occupies at time t .

4.1.5. Simulation Run Time

In our simulations, the number of cells in synthetic yeast colonies reaches $\approx 15,000$. Since our model requires computing the force between all cell pairs, the number of computational operations is proportional to the square of the number of cells. In order to decrease the computational cost of our simulations, we use a search algorithm that makes the number of computational operations asymptotically linear to the number of simulated cells. To do this, the total area occupied by cells is divided into S square subdomains. (Note these are the subdomains used for the nutrient model as described in Section 4.1.4). The size of the subdomains in simulations is determined based on the longest distance at which two cells can interact with each other. Since cell-cell adhesion and repulsion interactions are short range, the search algorithm for computing cell-cell interaction forces is limited to only neighboring subdomains. Since there are eight neighboring subdomains for each unique subdomain S_i , this algorithm reduces the total number of operations. In addition, the code for this work was implemented in C++ using OpenMP for parallelization. As a result, the total run-time of one simulation is ≈ 4 h on a 20-core node.

Table 1. Parameter Values Used in ABM. Descriptions of the biophysical and biological processes corresponding to these variables are detailed in Section 4.

Parameter	Symbol	Value	Units	Meaning	Reference
Poisson ratio	σ	0.3		Incompressibility of yeast cells	[38,50,74]
Young's Modulus	E	1000	kPa	Mechanical property of yeast cell walls	[38,50,74]
Receptor Surface Density	ϕ	10E15	m^{-2}	Density of surface adhesion molecules in the contact area	[38,50]
Single Bond Binding Energy	W_s	$25 k_B T$			[38,50]
E^{MB} Linear Spring Constant	K_{bud}	25	$nN/\mu m$	Attachment of bud on mother cell	calibrated
Damping Coefficient	η	2.5	$Ns/\mu m^2$	Viscosity of the growth media	[38,50]
Average Length of G2 phase	$G2_{avg}$	75	min		[82,83]
Average Length of G1 phase (new daughters)	$G1_{avg,daughter}$	120	min		[82,83]
Average Length of G1 phase (mothers)	$G1_{avg,mother}$	15	min		[82,83]
Average Mature Radius Size	R_{avg}	2.58	μm		[84]
Carrying Capacity	$M_{i,max}$	$18\pi R_{avg}^2$	μm^2	Maximal possible biomass for each subdomain	calibrated
Subdomain Size	$D_i(t)$	25	μm^2	Area of each subdomain	calibrated
Rate of Maximum Cell Cycle Adjustment	r	0.003		Controls the amount cell cycle is adjusted at each timestep	calibrated
Timestep	Δt	0.00144	min		calibrated

4.2. Colony Metrics

In this Section, we define the metrics used in Section 2 to analyze yeast colony morphology and organization. We first use two previously defined metrics to describe overall colony size and shape [41,42,44] and later introduce new metrics to characterize spatial organization of cells within the colony.

4.2.1. Colony Shape Metrics

The first two metrics are used to quantify the shape of the colony as it grows in time. The **colony expanse** quantifies how large the colony is, while the **colony sparsity** quantifies how circular the colony is. Both depend on the center of mass of the colony (Figure 15). Let $N(t)$ be the number of cells in the colony at time t , each of which has position $\vec{x}_i(t) = (x_i(t), y_i(t))$ and radius $R_i(t)$. Since we assume all cells are of the same type, the mass of each cell, $m_i(t)$, is proportional to the area of each cell with the same constant. As such, the center of mass of the colony at time t is given by the 2D point, $\vec{C}(t)$, defined by:

$$\text{Center of Mass: } \vec{C}(t) = \frac{\sum_{i=1}^{N(t)} m_i(t) \vec{x}_i(t)}{\sum_{i=1}^{N(t)} m_i(t)} = \frac{\sum_{i=1}^{N(t)} \pi R_i^2(t) \vec{x}_i(t)}{\sum_{i=1}^{N(t)} \pi R_i^2(t)}. \tag{13}$$

The colony expanse is defined as the largest distance between any cell boundary and the center of mass of the colony. That is:

$$\text{Colony Expanse: } E(t) = \max_{1 \leq i \leq N(t)} \left\{ \|\vec{x}_i(t) - \vec{C}(t)\| + R_i(t) \right\}. \tag{14}$$

The colony sparsity compares the area of the colony to the area of the circle with radius equal to the colony expanse. Notice that this circle need not be the smallest enclosing circle, as the smallest enclosing circle need not have its center at the colony center of mass, which is a modification of the colony sparsity used by Jönsson [41] and colony radius used by Aji [45]. In our simulations, cells do not overlap, so we define the area of the colony as follows:

$$\text{Area of Colony: } A_{colony}(t) = \sum_{i=1}^{N(t)} \pi R_i^2(t). \tag{15}$$

Thus, the colony sparsity is defined as:

$$\text{Colony Sparsity: } S(t) = \frac{\pi E(t)^2}{A_{\text{colony}}(t)}. \tag{16}$$

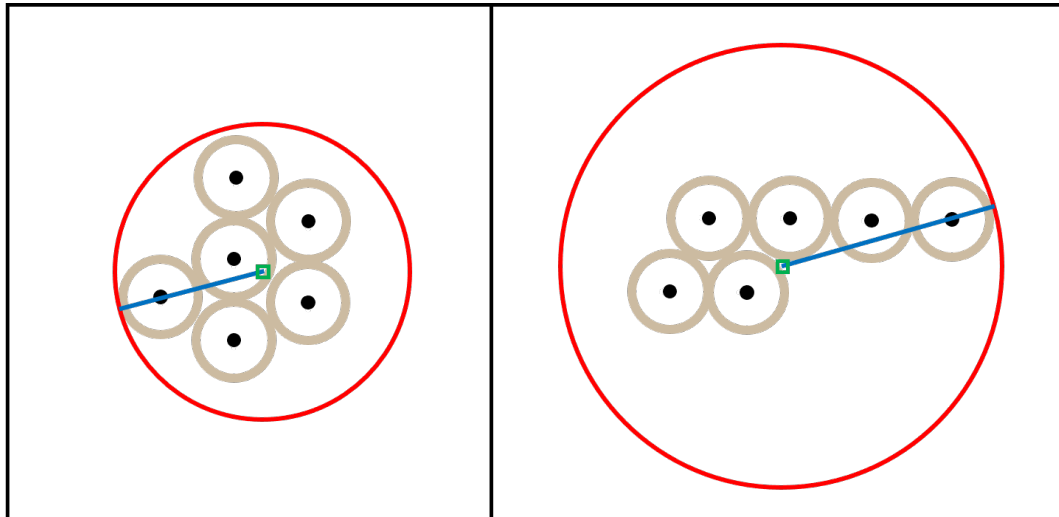


Figure 15. Colony Sparsity and Expanse. We first compute the colony center of mass (represented as a green square) using Equation (13). Then we determine the radius (length of the blue line) of the smallest circle which surrounds the entire colony centered at the center of mass (shown in red) using Equation (14). The colony sparsity is then computed using Equation (16) with the result of Equation (14), the area of the circle, and the total area of the cells using Equation (15). (Left): The space within the circle is more dense, thus covering more area within the circle with radius equal to the colony expanse, resulting in a small colony sparsity. (Right): The space that cells occupy within the circle is less dense, resulting in a higher colony sparsity.

4.2.2. Colony Organization Metrics

Next we introduce new metrics related to the organization of cells within the colony. We define a graph $G(V, E)$ as a set of nodes V and edges E . In each graph, all cells are represented as nodes. To analyze the colony organization, we consider two undirected graphs which evolve dynamically along with the colony (Figure 16). The first graph, G_S , is based on the Delaunay triangulation [85,86] and encodes spatial relationships between cells (Figure 16A). The second graph, the lineage graph which we denote as G_L , encodes mother-daughter relationships between cells (Figure 16B) Both graphs are constructed from the same vertex set, namely, all cells in the colony at time t :

$$V = \{c_1, c_2, \dots, c_{N(t)}\}.$$

The edge set E_S is constructed based on the Delaunay triangulation. The Delaunay triangulation is the dual graph of the Voronoi diagram for cell centers which consists of all points in the plane that are equidistant to their two nearest sites [87]. In our case, the edge set E_S is defined as:

$$E_S = \{(c_i, c_j) \mid \text{cell } i \text{ and } j \text{ share an edge in the Delaunay triangulation.}\}. \tag{17}$$

The edge set E_L consists of only edges between immediate mother-daughter cell pairs. Each cell, c_i , has a unique mother, $m(c_i)$. Thus, the edge set E_L consists of the following edges:

$$E_L = \{(c_i, m(c_i))\} \quad \text{for } i \in \{2, \dots, N(t)\}. \tag{18}$$

(Note that $m(c_1)$ is not defined because c_1 is the founder cell.)

Together $G_S = \{V, E_S\}$ and $G_L = \{V, E_L\}$ can be used to quantify how closely the spatial organization of the colony relates to mother-daughter cell pair interactions within the colony. To do this, we first define the intersection graph, G_I (Figure 16 C). G_I is constructed from the same vertex set containing all cells in the colony, but the edge set, E_I , only includes edges belonging to both E_S and E_L , namely:

$$E_I = E_S \cap E_L. \tag{19}$$

Our first colony organization metric, **colony connectivity**, is the fraction of mother-daughter edges that are also in the intersection graph:

$$\text{Colony Connectivity} := \frac{|E_I|}{|E_L|}. \tag{20}$$

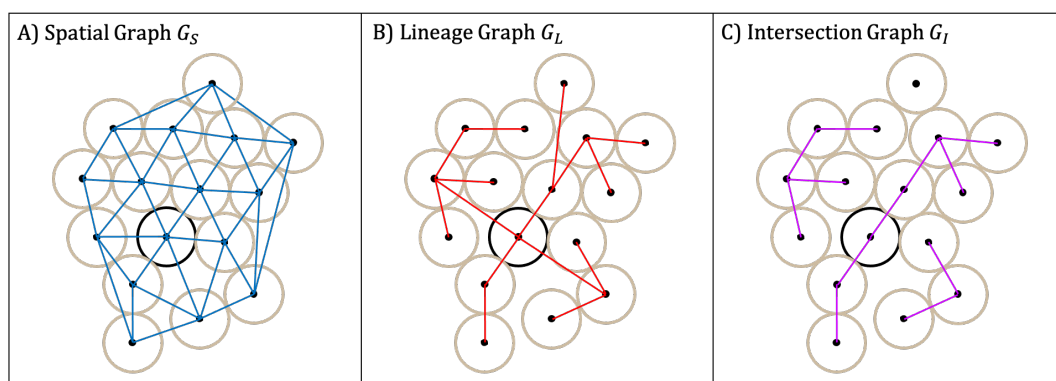


Figure 16. Colony Spatial Graphs. The vertex set for all three colony graphs is the same (all cell centers). The founder cell is designated in black. The edge set differs depending on the relationships between cells; (A): The edge set for the spatial graph G_S (blue edges) are those induced by the the Delaunay triangulation applied to the cell centers (Equation (17)); (B): The edges for the lineage graph G_L (red edges) correspond to mother-daughter pairs (Equation (18)); (C): The edge set for the intersection graph G_I (purple edges) include those edges that belong to the two previous edge sets (Equation (19)).

Our second organization requires us to establish a few concepts related to colony structure. First, we define a **subcolony** to be the subset of all cells whose common ancestor is an immediate daughter of the founder (Figure 17). We index the daughters of the founder cell by d_1, d_2, \dots, d_F where d_k denotes the k -th daughter of the founder cell. Note, every cell in the colony belongs to one of the subcolonies founded by an immediate daughter of the founder cell. Thus, for each $c_i \in V \setminus \{c_1\}$, we define $\text{Sub}(c_i)$ to be the subcolony that cell i belongs to. Moreover, each daughter of the founder is considered to be the founder of its own colony (i.e. a subcolony of the original colony) denoted $\text{Sub}(d_k)$ and the total number of subcolonies is equal to F , the total number of immediate daughters of the founder cell.

We next define a graph associated with each subcolony. Let V_{sub,d_k} be the set of all cells that are in $\text{Sub}(d_k)$. That is,

$$V_{\text{sub},d_k} = \{c_i \in V \setminus \{c_1\} \mid \text{Sub}(c_i) = \text{Sub}(d_k)\} \quad \text{for } i \in \{2, 3, \dots, N(t)\} \text{ and } k \in \{1, 2, \dots, F\}. \tag{21}$$

Let E_{sub,d_k} be the the set of all edges in E_S that join two cells in $\text{Sub}(d_k)$. Namely,

$$E_{\text{sub},d_k} = \{(c_i, c_j) \in E_S \mid \text{Sub}(c_i) = \text{Sub}(c_j) = \text{Sub}(d_k)\} \quad \text{for } i, j \in \{2, 3, \dots, N(t)\} \text{ and } i \neq j. \tag{22}$$

We define G_{sub,d_k} to be the subgraph of G_S whose vertex set is V_{sub,d_k} and whose edge set is E_{sub,d_k} (see Figure 17B,C). Note that E_{sub,d_k} for each k partitions the larger edge E_{sub} defined as:

$$E_{\text{sub}} = \bigcup_{k=1}^F E_{\text{sub},d_k}. \tag{23}$$

Similarly, V_{sub,d_k} for each k partitions the larger vertex set V_{sub} defined to be:

$$V_{\text{sub}} = \bigcup_{k=1}^F V_{\text{sub},d_k}. \tag{24}$$

We then define the **subcolony graph** $G_{\text{sub}}(V_{\text{sub}}, E_{\text{sub}})$, where

$$G_{\text{sub}} = \bigcup_{k=1}^F G_{\text{sub},d_k}. \tag{25}$$

We define our second colony organization metric to be the number of **connected components** of G_{sub,d_k} for each subcolony. A connected component is defined to be any maximal subgraph $G_{\text{connect}} \subseteq G_{\text{sub},d_k}$ such that any two vertices in G_{connect} are connected by a path and not connected to any other vertices in G_{sub} . The total number of connected components for the k^{th} subcolony is the total number of maximal subgraphs that partition the k^{th} subcolony graph G_{sub,d_k} .

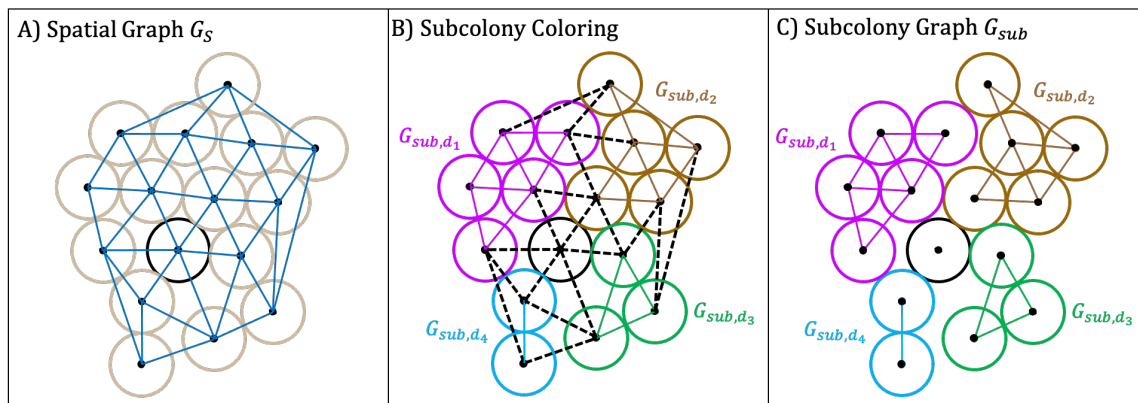


Figure 17. Constructing Subcolony Graphs. Subcolony graphs are constructed from partitions of the spatial graph G_S according to the following procedure. (A): We generate the the same spatial graph (G_S) using the Delaunay triangulation (Equation (17)). (The founder cell is indicated in black.) (B): We define a subcolony as a subset of cells in the lineage graph consisting of a daughter of the founder cell along with all of its descendants (Equation (21)). Edges are colored based one which subcolony each cell belongs to (Equation (22)). We then remove edges from the spatial connecting cells from different subcolonies (dotted black edges). (C): Removing these edges results in the subcolony graph G_{sub} , a set of subgraphs of G_S that we index by daughter cells: G_{sub,d_k} . These graphs preserve the spatial relationship between cells within the same subcolony (Equation (25)).

4.3. Statistical Analysis

To analyze the impact of budding and nutrient-limited growth on size, shape, and emergent patterns of spatial organization of cells, we generated 50 simulations of each colony type (budding/non-budding, nutrient-rich/nutrient-limited). To compare expanse, sparsity, connectivity and the number of connected components for each of the first five subcolonies between budding and non-budding colonies we used independent t -tests implemented using the `statannot` package in python [88]. In addition, we performed Kaplan-Meier survival analysis and generated

Kaplan-Meier survival curves using the lifelines library in python [89]. The survival function defines the probability that a death event (i.e. loss of a mother-daughter edge in G_S or a given subcolony splitting into more than 15 connected components) has not occurred yet at time t , or equivalently, the probability of surviving past time t [90]. We then used the log-rank test available in the lifelines library to compare the survival curves between budding and non-budding colonies in all cases (Figure 5D, Figure 6D, Figure 9D and Figure 10D). Finally, we computed the Kolmogorov-Smirnov statistic using the SciPy library in python [91] to compare the probability distributions of birth location between nutrient-rich and nutrient-limited colonies.

5. Conclusions

In this study, we introduced a novel two-dimensional, cell-based model describing the growth and movement, structure, and spatial organization of a colony of yeast cells to emphasize the importance of capturing budding behavior in these models. Our findings show that budding greatly impacts the local connectivity of a cell and that, together with nutrient limitation, acts to promote connected sectors with respect to the subcolony structure and produce highly variable subcolony sizes. Together, these findings offer novel interpretations and insights to observed sectoring phenotypes in yeast. We aim to investigate the multi-scale nature of these phenomena in future studies by extending our approach to include intracellular dynamics.

Author Contributions: Conceptualization, S.S. and M.B.-K.; methodology, S.S. and M.B.-K.; software, M.B.-K.; validation, M.B.-K., J.C. and S.S.; formal analysis, M.B.-K., J.C. and S.S.; investigation, M.B.-K.; resources, S.S.; data curation, M.B.-K.; writing-original draft preparation, M.B.-K., J.C. and S.S.; writing-review and editing, M.B.-K., J.C. and S.S.; visualization, M.B.-K.; supervision, S.S.; project administration, S.S.; funding acquisition, S.S. All authors have read and agree to the published version of the manuscript.

Funding: This research was by the Joint Initiative to Support Research at the Interface of the Biological and Mathematical Sciences between the National Science Foundation Division of Mathematical Sciences (NSF-DMS) and National Institutes of Health National Institute of General Medical Sciences (NIH-NIGMS) (Grant No. R01-GM126548) and used the Multi-Environment Computer for Exploration and Discovery (MERCED) cluster at UC Merced, funded by National Science Foundation Grant No. ACI-1429783.

Conflicts of Interest: The authors declare no conflict of interest.

Abbreviations

The following abbreviations are used in this manuscript:

ABM Agent-Based Model

References

1. DiSalvo, S.; Serio, T.R. Insights into prion biology: Integrating a protein misfolding pathway with its cellular environment. *Prion* **2011**, *5*, 76–83. [[CrossRef](#)] [[PubMed](#)]
2. Frazer, C.; Hernday, A.D.; Bennett, R.J. Monitoring Phenotypic Switching in *Candida albicans* and the Use of Next-Gen Fluorescence Reporters. *Curr. Protoc. Microbiol.* **2019**, *53*, e76. [[CrossRef](#)] [[PubMed](#)]
3. Klaips, C.L.; Hochstrasser, M.L.; Langlois, C.R.; Serio, T.R. Spatial quality control bypasses cell-based limitations on proteostasis to promote prion curing. *eLife* **2014**, *3*, e04288. [[CrossRef](#)] [[PubMed](#)]
4. Liebman, S.W.; Chernoff, Y.O. Prions in yeast. *Genetics* **2012**, *191*, 1041–1072. [[CrossRef](#)] [[PubMed](#)]
5. Giometto, A.; Nelson, D.R.; Murray, A.W. Physical interactions reduce the power of natural selection in growing yeast colonies. *Proc. Natl. Acad. Sci. USA* **2018**, *115*, 11448–11453. [[CrossRef](#)]
6. Ben-Jacob, E.; Schochet, O.; Tenenbaum, A.; Cohen, I.; Czirok, A.; Vicsek, T. Generic modelling of cooperative growth patterns in bacterial colonies. *Nature* **1994**, *368*, 46–49. [[CrossRef](#)]
7. Shapiro, J.A. The significances of bacterial colony patterns. *Bioessays* **1995**, *17*, 597–607. [[CrossRef](#)]
8. Mitri, S.; Clarke, E.; Foster, K.R. Resource limitation drives spatial organization in microbial groups. *ISME J.* **2016**, *10*, 1471–1482. [[CrossRef](#)]

9. Hallatschek, O.; Hersen, P.; Ramanathan, S.; Nelson, D.R. Genetic drift at expanding frontiers promotes gene segregation. *Proc. Natl. Acad. Sci. USA* **2007**, *104*, 19926–19930. [[CrossRef](#)]
10. Johnson, C.R.; Boerlijst, M.C. Selection at the level of the community: The importance of spatial structure. *Trends Ecol. Evol.* **2002**, *17*, 83–90. [[CrossRef](#)]
11. Hallatschek, O.; Nelson, D.R. Life at the front of an expanding population. *Evol. Int. J. Org. Evol.* **2010**, *64*, 193–206. [[CrossRef](#)] [[PubMed](#)]
12. Alber, M.S.; Jiang, Y.; Kiskowski, M.A. Lattice gas cellular automation model for rippling and aggregation in myxobacteria. *Phys. Nonlinear Phenom.* **2004**, *191*, 343–358. [[CrossRef](#)]
13. Amiri, A.; Harvey, C.; Buchmann, A.; Christley, S.; Shrout, J.D.; Aranson, I.S.; Alber, M. Reversals and collisions optimize protein exchange in bacterial swarms. *Phys. Rev. E* **2017**, *95*, 032408. [[CrossRef](#)] [[PubMed](#)]
14. Qin, B.; Fei, C.; Bridges, A.A.; Mashruwala, A.A.; Stone, H.A.; Wingreen, N.S.; Bassler, B.L. Cell position fates and collective fountain flow in bacterial biofilms revealed by light-sheet microscopy. *Science* **2020**, *369*, 71–77. [[CrossRef](#)] [[PubMed](#)]
15. Noble, S.M.; Gianetti, B.A.; Witchley, J.N. *Candida albicans* cell-type switching and functional plasticity in the mammalian host. *Nat. Rev. Microbiol.* **2017**, *15*, 96. [[CrossRef](#)] [[PubMed](#)]
16. Miller, M.G.; Johnson, A.D. White-opaque switching in *Candida albicans* is controlled by mating-type locus homeodomain proteins and allows efficient mating. *Cell* **2002**, *110*, 293–302. [[CrossRef](#)]
17. Lohse, M.B.; Johnson, A.D. White-opaque switching in *Candida albicans*. *Curr. Opin. Microbiol.* **2009**, *12*, 650–654. [[CrossRef](#)]
18. Lee, P.S.; Greenwell, P.W.; Dominska, M.; Gawel, M.; Hamilton, M.; Petes, T.D. A fine-structure map of spontaneous mitotic crossovers in the yeast *Saccharomyces cerevisiae*. *PLoS Genet.* **2009**, *5*, e1000410. [[CrossRef](#)]
19. Krafzig, D.; Klawonn, F.; Gutz, H. Theoretical analysis of the effects of mitotic crossover in large yeast populations. *Yeast* **1993**, *9*, 1093–1098. [[CrossRef](#)]
20. Ramírez-Zavala, B.; Reuß, O.; Park, Y.N.; Ohlsen, K.; Morschhäuser, J. Environmental induction of white-opaque switching in *Candida albicans*. *PLoS Pathog.* **2008**, *4*, e1000089. [[CrossRef](#)]
21. Xie, J.; Tao, L.; Nobile, C.J.; Tong, Y.; Guan, G.; Sun, Y.; Cao, C.; Hernday, A.D.; Johnson, A.D.; Zhang, L.; et al. White-opaque switching in natural MTL a/α isolates of *Candida albicans*: Evolutionary implications for roles in host adaptation, pathogenesis, and sex. *PLoS Biol.* **2013**, *11*, e1001525. [[CrossRef](#)] [[PubMed](#)]
22. Magno, R.; Grieneisen, V.A.; Marée, A.F. The biophysical nature of cells: Potential cell behaviours revealed by analytical and computational studies of cell surface mechanics. *BMC Biophys.* **2015**, *8*, 8. [[CrossRef](#)] [[PubMed](#)]
23. Cullen, P.J.; Sprague, G.F. The regulation of filamentous growth in yeast. *Genetics* **2012**, *190*, 23–49. [[CrossRef](#)]
24. Kron, S.J.; Styles, C.A.; Fink, G.R. Symmetric cell division in pseudohyphae of the yeast *Saccharomyces cerevisiae*. *Mol. Biol. Cell* **1994**, *5*, 1003–1022. [[CrossRef](#)] [[PubMed](#)]
25. Drubin, D.G.; Nelson, W.J. Origins of cell polarity. *Cell* **1996**, *84*, 335–344. [[CrossRef](#)]
26. Ni, L.; Snyder, M. A genomic study of the bipolar bud site selection pattern in *Saccharomyces cerevisiae*. *Mol. Biol. Cell* **2001**, *12*, 2147–2170. [[CrossRef](#)] [[PubMed](#)]
27. Chant, J.; Mischke, M.; Mitchell, E.; Herskowitz, I.; Pringle, J.R. Role of Bud3p in producing the axial budding pattern of yeast. *J. Cell Biol.* **1995**, *129*, 767–778. [[CrossRef](#)]
28. Byers, B. Cytology of the yeast life cycle. In *The Molecular Biology of The Yeast Saccharomyces: Life Cycle and Inheritance*; Springer: Berlin/Heidelberg, Germany, 1981; pp. 59–96.
29. Nadell, C.D.; Foster, K.R.; Xavier, J.B. Emergence of spatial structure in cell groups and the evolution of cooperation. *PLoS Comput. Biol.* **2010**, *6*, e1000716. [[CrossRef](#)]
30. Tam, A.; Green, J.E.F.; Balasuriya, S.; Tek, E.L.; Gardner, J.M.; Sundstrom, J.F.; Jiranek, V.; Binder, B.J. Nutrient-limited growth with non-linear cell diffusion as a mechanism for floral pattern formation in yeast biofilms. *J. Theor. Biol.* **2018**, *448*, 122–141. [[CrossRef](#)]
31. Gontar, A.; Bottema, M.J.; Binder, B.J.; Tronolone, H. Characterizing the shape patterns of dimorphic yeast pseudohyphae. *R. Soc. Open Sci.* **2018**, *5*, 180820. [[CrossRef](#)]
32. Tronolone, H.; Gardner, J.M.; Sundstrom, J.F.; Jiranek, V.; Oliver, S.G.; Binder, B.J. Quantifying the dominant growth mechanisms of dimorphic yeast using a lattice-based model. *J. R. Soc. Interface* **2017**, *14*, 20170314. [[CrossRef](#)] [[PubMed](#)]

33. Broach, J.R. Nutritional control of growth and development in yeast. *Genetics* **2012**, *192*, 73–105. [[CrossRef](#)] [[PubMed](#)]
34. Merchant, S.S.; Helmann, J.D. Elemental economy: Microbial strategies for optimizing growth in the face of nutrient limitation. In *Advances in Microbial Physiology*; Elsevier: Amsterdam, The Netherlands, 2012; Volume 60, pp. 91–210.
35. Plocek, V.; Váchová, L.; Šťovíček, V.; Palková, Z. Cell Distribution within Yeast Colonies and Colony Biofilms: How Structure Develops. *Int. J. Mol. Sci.* **2020**, *21*, 3873. [[CrossRef](#)] [[PubMed](#)]
36. Kayser, J.; Schreck, C.F.; Yu, Q.; Gralka, M.; Hallatschek, O. Emergence of evolutionary driving forces in pattern-forming microbial populations. *Philos. Trans. R. Soc. Biol. Sci.* **2018**, *373*, 20170106. [[CrossRef](#)]
37. Smith, W.P.; Davit, Y.; Osborne, J.M.; Kim, W.; Foster, K.R.; Pitt-Francis, J.M. Cell morphology drives spatial patterning in microbial communities. *Proc. Natl. Acad. Sci. USA* **2017**, *114*, E280–E286. [[CrossRef](#)] [[PubMed](#)]
38. Van Liedekerke, P.; Palm, M.; Jagiella, N.; Drasdo, D. Simulating tissue mechanics with agent-based models: concepts, perspectives and some novel results. *Comput. Part. Mech.* **2015**, *2*, 401–444. [[CrossRef](#)]
39. Glen, C.M.; Kemp, M.L.; Voit, E.O. Agent-based modeling of morphogenetic systems: Advantages and challenges. *PLOS Comput. Biol.* **2019**, *15*, e1006577. [[CrossRef](#)]
40. Gorochowski, T.E. Agent-based modelling in synthetic biology. *Essays Biochem.* **2016**, *60*, 325–336.
41. Jönsson, H.; Levchenko, A. An explicit spatial model of yeast microcolony growth. *Multiscale Model. Simul.* **2005**, *3*, 346–361. [[CrossRef](#)]
42. Wang, Y.; Lo, W.C.; Chou, C.S. A modeling study of budding yeast colony formation and its relationship to budding pattern and aging. *PLoS Comput. Biol.* **2017**, *13*, e1005843. [[CrossRef](#)]
43. Aprianti, D.; Haryanto, F.; Purqon, A.; Khotimah, S.; Viridi, S. Study of budding yeast colony formation and its characterizations by using circular granular cell. *J. Phys. Conf. Ser.* **2016**, *694*, 012079. [[CrossRef](#)]
44. Aprianti, D.; Khotimah, S.; Viridi, S. Budding yeast colony growth study based on circular granular cell. *J. Phys. Conf. Ser.* **2016**, *739*, 012026. [[CrossRef](#)]
45. Aji, D.P.P.; Aprianti, D.; Viridi, S. Stochastic Simulation of Yeast Cells and Its Colony Growth by Using Circular Granular Model for Cases of Growth and Birth Probabilities Depends on Position. *J. Phys. Conf. Ser.* **2019**, *1245*, 012010.
46. Purnama, F.A.; Meiriska, W.; Aji, D.P.P.; Aprianti, D.; Viridi, S. Network Analysis of *Saccharomyces cerevisiae*. *J. Phys. Conf. Ser.* **2019**, *1245*, 012081. [[CrossRef](#)]
47. Meiriska, W.; Purnama, F.; Aji, D.; Aprianti, D.; Viridi, S. Network Analysis of *Saccharomyces Cerevisiae* Colony: Relation between Spatial Position and Generation. *J. Phys. Conf. Ser.* **2019**, *1245*, 012006. [[CrossRef](#)]
48. Drasdo, D.; Loeffler, M. Individual-based models to growth and folding in one-layered tissues: intestinal crypts and early development. *Nonlinear Anal.-Theory Methods Appl.* **2001**, *47*, 245–256. [[CrossRef](#)]
49. Drasdo, D.; Forgacs, G. Modeling the interplay of generic and genetic mechanisms in cleavage, blastulation, and gastrulation. *Dev. Dyn. Off. Publ. Am. Assoc. Anat.* **2000**, *219*, 182–191. [[CrossRef](#)]
50. Drasdo, D.; Höhme, S. A single-cell-based model of tumor growth in vitro: Monolayers and spheroids. *Phys. Biol.* **2005**, *2*, 133. [[CrossRef](#)]
51. Drasdo, D.; Hoehme, S.; Block, M. On the role of physics in the growth and pattern formation of multi-cellular systems: What can we learn from individual-cell based models? *J. Stat. Phys.* **2007**, *128*, 287. [[CrossRef](#)]
52. Hornung, R.; Grünberger, A.; Westerwalbesloh, C.; Kohlheyer, D.; Gompper, G.; Elgeti, J. Quantitative modelling of nutrient-limited growth of bacterial colonies in microfluidic cultivation. *J. R. Soc. Interface* **2018**, *15*. [[CrossRef](#)]
53. Warren, M.R.; Sun, H.; Yan, Y.; Cremer, J.; Li, B.; Hwa, T. Spatiotemporal establishment of dense bacterial colonies growing on hard agar. *Elife* **2019**, *8*, e41093. [[CrossRef](#)] [[PubMed](#)]
54. De Virgilio, C. The essence of yeast quiescence. *FEMS Microbiol. Rev.* **2012**, *36*, 306–339. [[CrossRef](#)]
55. Herskowitz, I. Life cycle of the budding yeast *Saccharomyces cerevisiae*. *Microbiol. Rev.* **1988**, *52*, 536. [[CrossRef](#)]
56. Minois, N.; Frajnt, M.; Wilson, C.; Vaupel, J.W. Advances in measuring lifespan in the yeast *Saccharomyces cerevisiae*. *Proc. Natl. Acad. Sci. USA* **2005**, *102*, 402–406. [[CrossRef](#)] [[PubMed](#)]
57. Sheu, Y.J.; Barral, Y.; Snyder, M. Polarized growth controls cell shape and bipolar bud site selection in *Saccharomyces cerevisiae*. *Mol. Cell. Biol.* **2000**, *20*, 5235–5247. [[CrossRef](#)] [[PubMed](#)]
58. Mable, B. Ploidy evolution in the yeast *Saccharomyces cerevisiae*: A test of the nutrient limitation hypothesis. *J. Evol. Biol.* **2001**, *14*, 157–170. [[CrossRef](#)] [[PubMed](#)]

59. Serio, T.R. (The University of Chicago, Chicago, IL, USA). Personal Communication, 2020.
60. Binder, B.J.; Sundstrom, J.F.; Gardner, J.M.; Jiraneek, V.; Oliver, S.G. Quantifying two-dimensional filamentous and invasive growth spatial patterns in yeast colonies. *PLoS Comput. Biol.* **2015**, *11*, e1004070. [[CrossRef](#)]
61. Binder, B.J.; Simpson, M.J. Cell density and cell size dynamics during in vitro tissue growth experiments: Implications for mathematical models of collective cell behaviour. *Appl. Math. Model.* **2016**, *40*, 3438–3446. [[CrossRef](#)]
62. Ruiz-Riquelme, A.; Lau, H.H.; Stuart, E.; Goczi, A.N.; Wang, Z.; Schmitt-Ulms, G.; Watts, J.C. Prion-like propagation of β -amyloid aggregates in the absence of APP overexpression. *Acta Neuropathol. Commun.* **2018**, *6*, 26. [[CrossRef](#)]
63. Halfmann, R.; Jarosz, D.F.; Jones, S.K.; Chang, A.; Lancaster, A.K.; Lindquist, S. Prions are a common mechanism for phenotypic inheritance in wild yeasts. *Nature* **2012**, *482*, 363–368. [[CrossRef](#)]
64. Weinberg, R.P.; Koledova, V.V.; Shin, H.; Park, J.H.; Tan, Y.A.; Sinskey, A.J.; Sambanthamurthi, R.; Rha, C. Oil palm phenolics inhibit the in vitro aggregation of β -amyloid peptide into oligomeric complexes. *Int. J. Alzheimer's Dis.* **2018**, 2018.
65. Esler, W.P.; Stimson, E.R.; Jennings, J.M.; Vinters, H.V.; Ghilardi, J.R.; Lee, J.P.; Mantyh, P.W.; Maggio, J.E. Alzheimer's disease amyloid propagation by a template-dependent dock-lock mechanism. *Biochemistry* **2000**, *39*, 6288–6295. [[CrossRef](#)] [[PubMed](#)]
66. Brugger, S.D.; Baumberger, C.; Jost, M.; Jenni, W.; Brugger, U.; Mühlemann, K. Automated counting of bacterial colony forming units on agar plates. *PLoS ONE* **2012**, *7*, e33695. [[CrossRef](#)] [[PubMed](#)]
67. Bewes, J.; Suchowerska, N.; McKenzie, D. Automated cell colony counting and analysis using the circular Hough image transform algorithm (CHiTA). *Phys. Med. Biol.* **2008**, *53*, 5991. [[CrossRef](#)]
68. Ferrari, A.; Lombardi, S.; Signoroni, A. Bacterial colony counting with convolutional neural networks in digital microbiology imaging. *Pattern Recognit.* **2017**, *61*, 629–640. [[CrossRef](#)]
69. Scherz, R.; Shinder, V.; Engelberg, D. Anatomical analysis of *Saccharomyces cerevisiae* stalk-like structures reveals spatial organization and cell specialization. *J. Bacteriol.* **2001**, *183*, 5402–5413. [[CrossRef](#)]
70. Nguyen, B.; Upadhyaya, A.; van Oudenaarden, A.; Brenner, M.P. Elastic instability in growing yeast colonies. *Biophys. J.* **2004**, *86*, 2740–2747. [[CrossRef](#)]
71. Reynolds, T.B.; Fink, G.R. Bakers' yeast, a model for fungal biofilm formation. *Science* **2001**, *291*, 878–881. [[CrossRef](#)]
72. Brückner, S.; Mösch, H.U. Choosing the right lifestyle: Adhesion and development in *Saccharomyces cerevisiae*. *FEMS Microbiol. Rev.* **2012**, *36*, 25–58. [[CrossRef](#)]
73. Dranginis, A.M.; Rauceo, J.M.; Coronado, J.E.; Lipke, P.N. A biochemical guide to yeast adhesins: Glycoproteins for social and antisocial occasions. *Microbiol. Mol. Biol. Rev.* **2007**, *71*, 282–294. [[CrossRef](#)]
74. Smith, A.E.; Zhang, Z.; Thomas, C.R.; Moxham, K.E.; Middelberg, A.P. The mechanical properties of *Saccharomyces cerevisiae*. *Proc. Natl. Acad. Sci. USA* **2000**, *97*, 9871–9874. [[CrossRef](#)]
75. Stenson, J.D.; Hartley, P.; Wang, C.; Thomas, C.R. Determining the mechanical properties of yeast cell walls. *Biotechnol. Prog.* **2011**, *27*, 505–512. [[CrossRef](#)] [[PubMed](#)]
76. Hoehme, S.; Drasdo, D. A cell-based simulation software for multi-cellular systems. *Bioinformatics* **2010**, *26*, 2641–2642. [[CrossRef](#)] [[PubMed](#)]
77. Byrne, H.; Drasdo, D. Individual-based and continuum models of growing cell populations: A comparison. *J. Math. Biol.* **2009**, *58*, 657. [[CrossRef](#)] [[PubMed](#)]
78. Farhadifar, R.; Röper, J.C.; Aigouy, B.; Eaton, S.; Jülicher, F. The influence of cell mechanics, cell-cell interactions, and proliferation on epithelial packing. *Curr. Biol.* **2007**, *17*, 2095–2104. [[CrossRef](#)] [[PubMed](#)]
79. Kursawe, J.; Brodskiy, P.A.; Zartman, J.J.; Baker, R.E.; Fletcher, A.G. Capabilities and Limitations of Tissue Size Control through Passive Mechanical Forces. *PLoS Comput. Biol.* **2015**, *11*, e1004679. [[CrossRef](#)] [[PubMed](#)]
80. Newman, T.J. Modeling multicellular systems using subcellular elements. *Math. Biosci. Eng.* **2005**, *2*, 613–624. [[CrossRef](#)]
81. Brewer, B.J.; Chlebowicz-Sledziewska, E.; Fangman, W.L. Cell cycle phases in the unequal mother/daughter cell cycles of *Saccharomyces cerevisiae*. *Mol. Cell. Biol.* **1984**, *4*, 2529–2531. [[CrossRef](#)]
82. Di Talia, S.; Skotheim, J.M.; Bean, J.M.; Siggia, E.D.; Cross, F.R. The effects of molecular noise and size control on variability in the budding yeast cell cycle. *Nature* **2007**, *448*, 947–951. [[CrossRef](#)]
83. Váchová, L.; Palková, Z. How structured yeast multicellular communities live, age and die? *FEMS Yeast Res.* **2018**, *18*, foy033. [[CrossRef](#)]

84. Milani, M.; Batani, D.; Bortolotto, F.; Botto, C.; Baroni, G.; Cozzi, S.; Masini, A.; Ferraro, L.; Previdi, F.; Ballerini, M.; et al. *Differential Two Colour X-ray Radiobiology of Membrane/Cytoplasm Yeast Cells: TMR Large-Scale Facilities Access Programme*; NASA: Washington, DC, USA, 1998.
85. Finch, A.M.; Wilson, R.C.; Hancock, E.R. Matching delaunay graphs. *Pattern Recognit.* **1997**, *30*, 123–140. [[CrossRef](#)]
86. Lee, D.T.; Schachter, B.J. Two algorithms for constructing a Delaunay triangulation. *Int. J. Comput. Inf. Sci.* **1980**, *9*, 219–242. [[CrossRef](#)]
87. Weatherill, N.P.; Hassan, O. Efficient three-dimensional Delaunay triangulation with automatic point creation and imposed boundary constraints. *Int. J. Numer. Methods Eng.* **1994**, *37*, 2005–2039. [[CrossRef](#)]
88. Weier, M.H. Wal-Mart Chooses Neoview Data Warehouse. 2007. Available online: <http://www.informationweek.com/news/201202317> (accessed on 2 April 2020)
89. Davidson-Pilon, C.; Kalderstam, J.; Jacobson, N.; Kuhn, B.; Zivich, P.; Williamson, M.; Abdeali, J.K.; Datta, D.; Fiore-Gartland, A.; Parij, A.; et al. *CamDavidsonPilon/lifelines: v0.24.16*; Zenodo: Genève, Switzerland, 2020. [[CrossRef](#)]
90. Efron, B. Logistic regression, survival analysis, and the Kaplan-Meier curve. *J. Am. Stat. Assoc.* **1988**, *83*, 414–425. [[CrossRef](#)]
91. Virtanen, P.; Gommers, R.; Oliphant, T.E.; Haberland, M.; Reddy, T.; Cournapeau, D.; Burovski, E.; Peterson, P.; Weckesser, W.; Bright, J.; et al. SciPy 1.0: Fundamental Algorithms for Scientific Computing in Python. *Nat. Methods* **2020**, *17*, 261–272. [[CrossRef](#)]



© 2020 by the authors. Licensee MDPI, Basel, Switzerland. This article is an open access article distributed under the terms and conditions of the Creative Commons Attribution (CC BY) license (<http://creativecommons.org/licenses/by/4.0/>).